Correspondence to:
Y. Liu, and J. J. Jiao,
yliu3867@uwo.ca
jjiao@hku.hk

Spatial Characteristics Reveal the Reactive Transport of Radium Isotopes (^{224}Ra, ^{223}Ra, and ^{228}Ra) in an Intertidal Aquifer

Yi Liu[1,2,3], Jiu Jimmy Jiao[1,2], Rong Mao[1,2], Xin Luo[1,2], Wenzhao Liang[1,2], and Clare E. Robinson[3]

[1]Department of Earth Sciences, The University of Hong Kong, Hong Kong, China, [2]Shenzhen Research Institute, The University of Hong Kong, Shenzhen, China, [3]Department of Civil and Environmental Engineering, Western University, London, Ontario, Canada

Abstract This study presents high-resolution two-dimensional distributions of radium isotopes in the shallow intertidal aquifer of Tolo Harbor, Hong Kong, illustrating the importance of salinity, groundwater residence time, and tidal flushing and mixing in controlling radium behavior in the system. The activities of radium isotopes are low in the fresh groundwater zone with activities increasing in the transition zone (1 < salinity < 25) due to desorption of radium from sediment surface coatings. In the high salinity zone (salinity > 25), the activities of radium isotopes increase with depth due to tidal flushing and mixing of the recirculating seawater in the shallow aquifer as well as increasing residence time with depth. The dissolved radium isotopes are identified to be in disequilibrium in shallow intertidal aquifer based on radium isotopic ratios and observed depletion of dissolved radium isotopes compared to the theoretical mixing line between the equilibrium activity and fresh groundwater. The influence of continuous tidal flushing of the shallow intertidal aquifer on radium is revealed, and shallow sediments are observed to have less total exchangeable radium isotopes than deeper in the aquifer. A new one-dimensional reactive transport model that considers a depth-dependent production rate is applied to simulate the vertical distribution of radium isotopes in the intertidal aquifer as seawater infiltrates the beach. Using least squares fitting of the model to field data, the vertical infiltration seepage velocity is estimated to be ~0.5 m/day, and the dimensionless adsorption partition coefficient of radium isotopes (K) is 350. This agrees well with K values (202–365) calculated using an adsorption/desorption model as well as measured values (266 in February and 205 in April). Based on the spatial distribution of radium isotopes and flow patterns in the intertidal aquifer, groundwater in Ra disequilibrium zone is recommended as the endmember for tide- or wave-driven submarine groundwater discharge (SGD) that has shallow flow paths, and groundwater in Ra equilibrium zone is recommended as endmember for seasonally driven or density-driven SGD that has deep flow paths.

1. Introduction

Naturally occurring radium isotopes (^{224}Ra, ^{223}Ra, ^{228}Ra, and ^{226}Ra) have been widely used over the last few decades to estimate submarine groundwater discharge (SGD) and associated chemical inputs to the ocean (Burnett et al., 2006; Charette & Buesseler, 2004; Moore, 1996). Mass balance model-based methods are commonly applied to estimate volumetric SGD rates from radium isotope field data (Burnett et al., 2006; Moore, 2010). A key uncertainty in using these methods is selecting a representative saline groundwater endmember for use in model. Endmember selection is challenging due to the high natural variability of radium activity in the subsurface and also because total SGD is composed of different components including fresh groundwater discharge as well as seawater recirculating across the sediment-water interface due to oceanic forces including tides and waves (Li et al., 1999; Robinson et al., 2007; Tao et al., 2019). Cho and Kim (2016) determined that simply applying an average radium activity of randomly sampled coastal groundwater as an endmember without considering the effect of salinity may lead to twofold to threefold overestimation of SGD at the global scale. Improved understanding of the behavior of radium isotopes in intertidal aquifers including their spatial distribution is needed to reduce uncertainties associated with groundwater endmember selection and subsequently to obtain more accurate SGD estimates when applying radium mass balance models.

It is well established that the intertidal aquifer, which represents an important transition zone between the land and ocean, is a zone of high biogeochemical reactivity and plays a key role in processing chemical constituents including carbon (Moore, 1999; Santos et al., 2009), trace metals (Charette & Sholkovitz, 2006; McAllister et al., 2015; Rouxel et al., 2008), and nutrients (Gonneea & Charette, 2014; Santos et al., 2008). The geochemical conditions in an intertidal aquifer including the salinity, pH, dissolved oxygen, temperature, and oxidation-reduction potential (ORP) are spatially complex and vary over diurnal to seasonal scales due to forces such as tides, waves, seasonal hydrologic variations, and changes in the beach morphology (Liu, Jiao, & Liang, 2018; Liu, Liang, & Jiao, 2018; O'Connor et al., 2018; Robinson et al., 2018). The distribution of radium isotopes in an intertidal aquifer is also complex and can vary considerably in response to changes in hydrodynamics, redox conditions, salinity, pH, and availability of solid phases to which radium associates (e.g., Fe and Mn oxides; Gonneea et al., 2013; Heiss et al., 2017; Liu, Jiao, Liang, & Kuang, 2017; Liu et al., 2016, 2019; McAllister et al., 2015). For example, radium partitioning between the solid phase and the dissolved phase decreases with increasing salinity due to the increase in ionic strength (Beck & Cochran, 2013; Kiro et al., 2014; Swarzenski, 2007). Changes in the redox condition also affect radium partitioning by modifying the stability of solid phases such as Fe and Mn oxides that have strong affinity for radium isotopes (Beck & Cochran, 2013; Charette & Sholkovitz, 2006; Gonneea et al., 2013). O'Connor et al. (2018) recently found seasonal temperature and dissolved organic carbon availability to be key factors controlling the cycling and distribution of Fe and Mn in the intertidal aquifer. pH also affects radium partitioning between the solid phase and the dissolved phase as it affects competitive cation sorption processes as well as the stability of Fe and Mn oxides. A positive correlation between pH and the radium partitioning coefficient was observed by Beck and Cochran (2013). In addition, in barium- and sulfate-rich coastal groundwater systems such as the Dead Sea (Kiro et al., 2013) and Waquoit Bay (Gonneea et al., 2013), it has been shown that radium can be removed via coprecipitation with barium in a form of barite or celestine.

Prior studies have characterized the distribution of radium isotopes in nearshore aquifers to better understand the behavior of the isotopes and address uncertainties associated with selecting a suitable groundwater endmember for estimating SGD volumes. For example, by characterizing the spatial distribution of radium activity in a nearshore aquifer, Michael et al. (2011) clearly illustrated the complex behavior of radium isotopes with activities distinctively different in the fresh groundwater, salt-wedge, and upper saline plume zones. The spatial distributions of the radium isotopes were found to be associated with aquifer heterogeneity, groundwater flow paths, and associated residence time scales in each zone of the nearshore aquifer. This study provided valuable insight into the radium isotope behavior in a nearshore aquifer and subsurface flow processes driving SGD; however, this study did not show the spatial variation in radium activity within each zone. Michael et al. (2011) did not explore the influences of tidal flushing which is important for tidally dominated coastlines. Radium isotopes have also been observed to vary considerably over seasonal and interannual time scales in the coastal groundwater of Waquoit Bay, MA (Gonneea et al., 2013) and the Mediterranean Sea, Barcelona (Cerdà-Domènech et al., 2017). Several to tenfold temporal variations in radium isotope activities were attributed to changing hydrologic forces inducing shifts in the seawater-freshwater interface and subsequent exchange of radium between the dissolved phase and solid surface coatings. These studies evaluating the long-term variations in radium isotopes used only one observation piezometer and therefore did not explore variations in the distribution of radium isotopes across the intertidal aquifer although geochemical reactions are known to have clear spatial patterns linked to the groundwater flow patterns and origins of the water (Robinson et al., 2007; Santos et al., 2012). More recently, Liu, Jiao, Liang, and Luo (2018) conducted high spatial resolution sampling across the transition zone of the intertidal aquifer in Tolo Harbor, Hong Kong, illustrating the dissimilar behavior of the radium isotopes in the different zones of the transition zone and identifying that radium isotopes are comparatively low in the upper saline plume compared to the salt-wedge due to short groundwater residence times. The focus of Liu, Jiao, and Liang (2018) was evaluating the short-term variations in radium isotopes induced by semidiurnal tidal fluctuations and the implications of these variations on other chemical constituents. Importantly, this study showed that the relationship between radium isotopes and other chemicals (e.g., inorganic carbon, trace metal, and nutrients) varies across the transition zone. Liu, Jiao, and Liang (2018) was conducted at the same location as this current study but only measured radium activities in the transition zone of the intertidal

aquifer which is approximately 20 m wide in the cross-shore direction and covers less than 20% of the intertidal aquifer and only a small portion of the discharge zone. Therefore, it is challenging to provide recommendations for groundwater endmember selection based on this study. In addition, Liu, Jiao, and Liang (2018) did not consider the effects of tidal flushing (herein "flushing" represents the process by which infiltrating seawater leaches radium from the sediments) and mixing (herein "mixing" represents the dilution of original saline groundwater by newly infiltrating seawater) which are important processes in the shallow intertidal aquifer and may play an important role in controlling the distribution of radium isotopes in the solid and dissolved phases. Therefore, investigation of radium isotopes across the entire intertidal aquifer (including the fresh groundwater, salt-wedge, and upper saline plume zones) is needed to fully understand radium behavior in the intertidal aquifer.

The distribution of radium isotopes in a nearshore aquifer depends on the groundwater flow patterns, groundwater residence time, and salinity in the different zones of the aquifer. These zones change in response to varying hydrologic conditions (e.g., changing tidal, spring-neap, wave, and seasonal forces; Abarca et al., 2013; Heiss & Michael, 2014; Liu et al., 2016). Previous studies evaluating the transport of radium isotopes in inland (Krest & Harvey, 2003; Tricca et al., 2001) and coastal aquifers (Kiro et al., 2012; Kiro et al., 2013; Michael et al., 2011) have applied a one-dimensional diagenetic reactive transport model of radium isotopes with constant production rates in the aquifer. However, our data indicate that this model may not be appropriate for simulating the production radium isotopes in an intertidal aquifer due to aquifer heterogeneity and frequent tidal flushing of shallow aquifer sediments. Based on our data, we develop a new one-dimensional diagenetic reactive transport model that considers depth-dependent production rates to simulate the vertical transport of radium isotopes in the intertidal aquifer from the beach surface. By using depth-dependent production rates this model is the first to consider the effects of tidal flushing on aquifer heterogeneity and the subsequent transport and ingrowth of radium isotopes in the intertidal aquifer. The spatial distribution in the entire intertidal aquifer and simulated radium processes provide important new conceptual understanding of the distribution and ingrowth of radium isotopes in the intertidal aquifer as needed to inform groundwater endmember selection for accurate estimation of SGD and associated chemical fluxes to the ocean.

In this study, high-resolution field data are presented together with a new one-dimensional diagenetic transport radium model to investigate factors controlling the distribution of radium in an intertidal aquifer and provide guidance for groundwater-member selection. The paper addresses the following key research questions: (1) What is the spatial distribution and zonation of radium isotopes in the intertidal aquifer? (2) What are the factors influencing the zonation of radium isotopes in the intertidal aquifer and partitioning between the adsorbed and dissolved phases? (3) How does tidal flushing affect the spatial distribution of radium isotopes? (4) How should groundwater endmembers be selected in the intertidal aquifer for application in radium mass balance models used to estimated SGD volumes.

2. Material and Methods

2.1. Study Site

Tolo Harbor, located in the northeast of New Territories, Hong Kong, is a semiclosed embayment with a surface area of 50 km^2 and a shoreline of 82 km (Figure 1a). The study site (22°28′06.91″N, 114°13′02.22″E) is located at Ting Kok beach in Tolo Harbor (Figure 1b). The annual mean precipitation for this region is ~2,030 mm (Lee et al., 2012; Luo et al., 2014) with the monthly precipitation and temperature variations in 2015 and 2016 shown in Figure 1c. Details of the field study site are provided in Liu, Jiao, Liang, and Luo (2017) with a brief overview provided here. The semidiurnal tide has a mean sea level of 1.45 mPD (meter above Principal Datum) and an average tidal range of 1.06 m (Liu, Jiao, Liang, & Kuang, 2017). The averaged wind speed in February and April 2016 are 11.3 and 9.0 km/hr, respectively, and the prevailing wind direction is 60° northeast. As the field site is sheltered and located on the north side of the harbor, the wave conditions are calm, and wave effects on the nearshore aquifer are minor relative to tidal forcing. The sediments above the Middle Jurassic-Lower Cretaceous volcanic bedrock mainly contain silt, clay, shell fragment, and sand with different grain sizes. More than 60% of sediments have a grain size smaller than 500 μm, more than 30% of sediments have a grain size smaller than 290 μm, and the sediment is well-sorted gravelly sand according to Unified Soil Classification system (Liu, Jiao, & Cheng, 2018). The vertical hydraulic conductivity was measured to be 4.5 ± 0.4 m/day and 1.6 ± 0.5 m/day in shallow bare sandy beach and
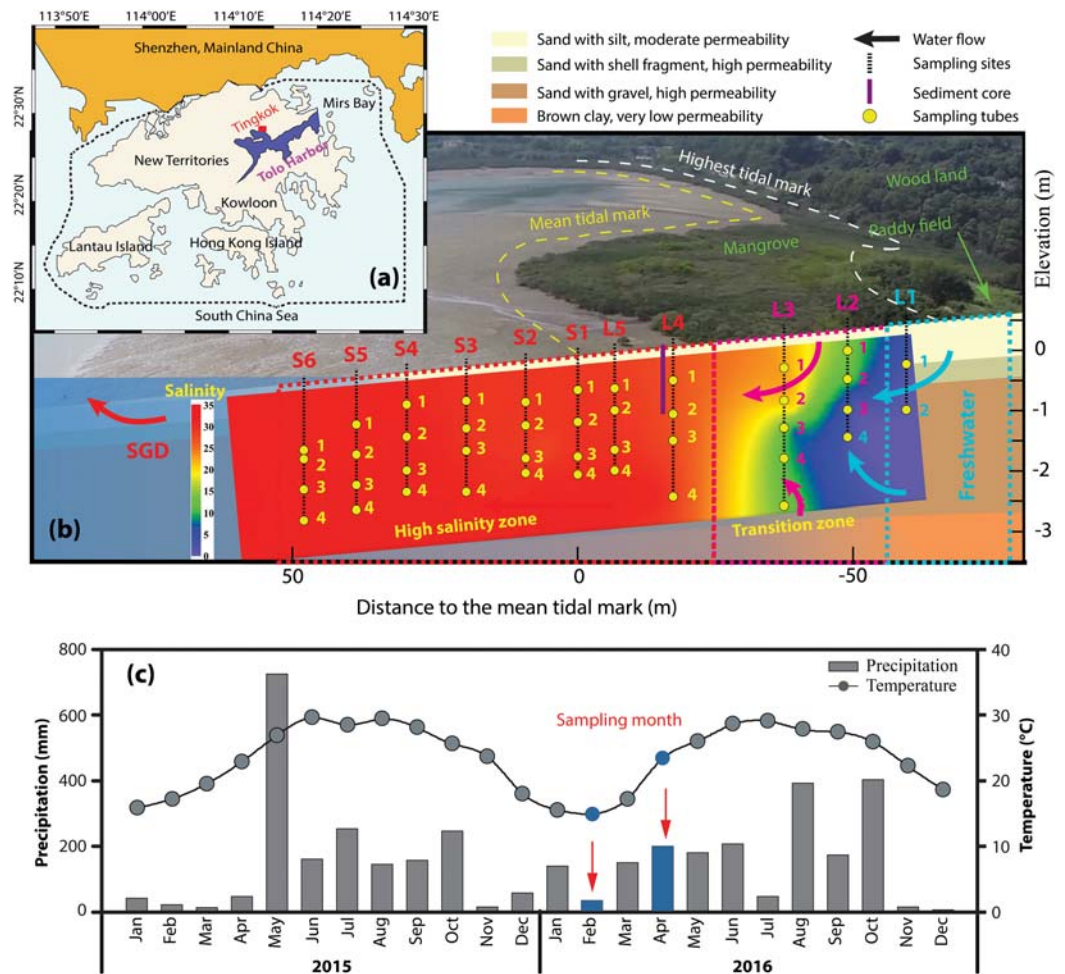
Figure 1. (a) The locations of Tolo Harbor and study site, (b) the location of permanent multilevel sampling tubes in the sandy aquifer near Ting Kok, and (c) the monthly precipitation and temperature in 2015 and 2016. Note that (a) and (b) are modified from Liu, Jiao, Liang, and Kuang (2017) and (c) is modified from Liu, Jiao, Liang, and Luo (2017). The red-blue color contours indicate the salinity distribution in February 2017, and the color scale is shown on the left (Liu, Jiao, Liang, & Kuang, 2017). Three zones, that is, high salinity zone (red), transition zone (between blue and red), and fresh groundwater zone (blue), are identified according to the salinity distribution. The data in (c) are from the nearest (about 500 m) meteorology station (http://www.hko.gov.hk/cis/climat_c.htm).

mangrove zone, respectively (Liu, Jiao, & Cheng, 2018). The porosity is measured to be 0.3 using a standard method (Fetter, 2000). The horizontal hydraulic gradient in the fresh groundwater zone (above the highest tidal mark) varies seasonally but is estimated to be approximately 0.05 in April 2016 based on groundwater level data (Liu, Jiao, & Cheng, 2018). The slope of the sandy beach is ~1%. The composition of the coastal aquifer below 3 m is not known as we were not able to drill more than 3 m below the surface using our simple drilling method.

A permanent multilevel sampling system (Luo et al., 2017) was installed along a transect perpendicular to the shoreline in the intertidal aquifer to obtain high-resolution spatial distributions of dissolved radium isotopes and other chemical constituents (Liu, Jiao, Liang, & Kuang, 2017). The system consists of 11 sampling sites with L1 to L5 above the mean tidal mark and S1 to S6 below the mean tidal mark (Figure 1b). Each sampling site has two to five sampling tubes with inlet ports located at different depths below the ground surface. Each sampling tube is denoted by a combination of a site number and a tube number. For example, L1-1 is the shallowest sampling port at sampling site L1; L3-5 is the deepest sampling port at site L3. The locations of the sampling ports are shown in Figure 1b with the depths of all sampling ports provided in Supporting Information Table S1.

The spatial distribution of salinity (S), pH, and ORP in February and April 2016 was described in a previous study at the same site (Liu, Liang, & Jiao, 2018). The salinity distribution for February 2017 is shown in Figure 1 with additional salinity, pH, and ORP data provided in the Supporting Information. According to the stable isotope (Liu, Jiao, Liang, & Luo, 2017), salinity (Liu, Liang, & Jiao, 2018), and radium isotopes data (Liu, Jiao, Liang, & Luo, 2018) in February and April, the flow patterns in the intertidal aquifer can be generalized as illustrated in Figure 1b. Specifically, the intertidal aquifer can be divided three distinct zones based on the salinity data: fresh groundwater zone (L1, L2-3, and L2-4 with $S < 1$), transition zone (L2 and L3 with $1 < S < 25$), and high salinity zone (L3 to S5 with $S > 25$). In the fresh groundwater zone, shallow (L1) and deep (L2-3 and L2-4) fresh groundwater are further differentiated based on stable isotopes data. In addition, the L3-5 is recognized l to be located in the transition zone of salt-wedge since it has the highest radium activity but comparatively low salinity compared to other locations such as L3-1 and L3-2. The deep fresh groundwater is oxic with low pH, and the shallow fresh groundwater is slightly reduced with higher pH. Groundwater in the transition zone and high salinity zone is reduced. The near-surface area of the salinity transition zone (<1.0 m) is highly reduced (ORP < −150 mV; Figure S1).

2.2. Sampling and Analysis

Groundwater samples were collected on 24 February and 25 April 2016. Ancillary parameters including salinity, pH, and ORP were measured in situ immediately after the sample collection with a portable multiparameter meter (HI 98194, Hanna Instruments). The resolutions and the accuracies of pH, ORP, and salinity are 0.01 and ±0.02, 0.1 and ±1.0 mV, and 0.01 and ±0.01, respectively. Between 0.5 and 1.5 L of groundwater was pumped from each sampling tube and transported to laboratory within 3 hr. On arrival at the laboratory, samples were filtered (1 μm column filter). Radium isotopes were extracted from the groundwater by pumping the sample through manganese-coated acrylic fibers (Mn-fiber) with a flow rate <1 L/min (Moore, 2008). Radium isotopes were measured using a radium delayed coincidence counters (RaDeCC) system (Moore & Arnold, 1996). The prepared Mn-fiber was placed in the closed loop of RaDeCC system to measure ^{224}Ra activity within 3 days of sample collection. The sample was recounted 10 and 25 days later to measure ^{223}Ra and ^{228}Th, respectively. ^{228}Th activity was applied to obtain excess ^{224}Ra activity (named ^{224}Ra hereafter). About 1–1.5 years later, ^{228}Ra was measured using the RaDeCC system following the standard procedure described in Moore (2008). The ^{228}Ra was calculated using the equation:

$$^{228}_{i}\text{Ra} = \frac{^{228}_{m}\text{Th} - \left[^{228}_{i}\text{Th} \times e^{-\lambda_{\text{Ra}}t - (-\lambda_{\text{Th}}t)}\right]}{1.499 \times e^{-\lambda_{\text{Ra}}t - (-\lambda_{\text{Th}}t)}}, \tag{1}$$

where $^{228}_{i}$Ra, $^{228}_{m}$Th, and $^{228}_{i}$Th are the initial activity of ^{228}Ra, measured activity of ^{228}Th (measured at 1–1.5 years), and initial activity of ^{228}Th (~25 days), respectively. λ_{Ra} and λ_{Th} are the decay constants of ^{228}Ra and ^{228}Th, respectively. t is the ingrowth time. The uncertainties associated with the measurement of ^{224}Ra and ^{223}Ra via RaDeCC were estimated according to Garcia-Solsona et al. (2008). The ^{228}Ra uncertainties were calculated based on the uncertainties of $^{228}_{m}$Th and $^{228}_{i}$Th and using error propagation rules.

In addition to groundwater sampling, one sediment core (1 m deep) was collected near L4 to measure the total exchangeable ^{224}Ra (total ^{224}Ra in the dissolved phase and surface coating of sediments). The total exchangeable ^{224}Ra in bulk sediment was determined following the method described in Cai et al. (2012). Briefly, the sediment core was sliced into 2 cm intervals, and the sediment at a target depth was placed in a glass beaker; 250 ml deionized water was added to form a slurry which was then ultrasonicated for 5 min. Concentrated NH$_3$·H$_2$O was then added to the slurry to adjust pH. Following this, KMnO$_4$ (1.0 ml, 3.0 g/L) and MnCl$_2$ (1.0 ml, 8.0 g/L) solutions were added to produce suspended MnO$_2$ particles to coprecipitate Ra in the interstitial water. Finally, the sediment slurry was filtered onto a 142 mm of GF/F filter. After adjusting the moisture of samples to obtain a water/sediment ratio of 0.4–0.5, the bulk sediment ^{224}Ra was measured using the RaDeCC system (Cai et al., 2012). Five standards with addition of different known activities of ^{232}Th standard solution were made following the procedure described previously by Cai et al. (2012). The calibration curve for the bulk sediment ^{224}Ra was determined by measuring six standards (five standards with addition of known ^{232}Th plus one sediment sample without addition of ^{232}Th) using the

RaDeCC system (Cai et al., 2012). The efficiency of each channel of the RaDeCC system was determined by measuring the six standards, respectively. The uncertainties of the standard measurement are 3.9–5.2%, and the overall accuracy of the measurement is within ±4.5%.

3. Results

3.1. ^{224}Ra

The spatial distributions of ^{224}Ra in February and April are presented in Figure 2a. The ^{224}Ra activities in the fresh groundwater are relatively low with values ranging from 2.84 ± 0.08 to 4.69 ± 0.20 dpm/L and 0.82 ± 0.03 to 0.97 ± 0.04 dpm/L in February and April, respectively (Tables S1 and S2). The lower ^{224}Ra activity in the fresh groundwater in April compared with February is due to a decrease in the groundwater salinity in the fresh groundwater zone (Tables S1 and S2) which increases the adsorption of ^{224}Ra onto surface sediment coatings. The decrease in groundwater salinity in April compared with February is due to heavy seasonal rainfall (Figure 1c) which would have increased the inland groundwater level and fresh groundwater discharge through the intertidal aquifer. In addition, as shown by Liu et al. (2016) and Robinson et al. (2007), the increase in fresh groundwater discharge weakens the tide-induced seawater recirculation through the intertidal zone and causes the upper saline plume to contract. This leads to shorter residence times for the tide-induced recirculation (Robinson et al., 2007), which results in lower ^{224}Ra activity across the entire intertidal zone in April compared to February. As can be seen in Figure 2a, ^{224}Ra activity is higher in the transition zone (−40 to −20 m lateral distance to mean tidal mark, negative values denote the landward direction) compared to the fresh groundwater zone due to the increase in salinity and ionic strength which promotes ^{224}Ra desorption from the sediment surface coatings (Kiro et al., 2012; Webster et al., 1995). The ^{224}Ra activities in the transition zone decrease slightly from February to April (Tables S1 and S2) with the activities varying from 11.5 ± 0.4 to 67.4 ± 1.7 dpm/L and 4.36 ± 0.16 to 62.2 ± 2.0 dpm/L, respectively. Importantly, the maximum ^{224}Ra activity in the transition zone (L2-L3 area) was observed at L3-5 where the salinity was ~10. The ^{224}Ra activity was higher than other locations in the transition zone that have higher salinity (e.g., L3-1 and L3-2) despite higher salinity typically causing greater ^{224}Ra desorption from the sediment surface coatings and thus high dissolved phase activities. This result is consistent with our previous study (Liu, Jiao, Liang, & Luo, 2018) and is likely because the more saline groundwater at the shallower locations (L3-1 and L3-2) has a shorter residence time and high mixing (dilution) with newly infiltrating seawater. In contrast, the deeper groundwater in the transition zone may be upwelling from the salt-wedge with a long residence time and negligible mixing loss. In the high salinity zone (L4 to S6), ^{224}Ra activities are much higher than in the fresh groundwater zone and transition zone ranging from 73.5 ± 1.8 to 280.6 ± 6.4 dpm/L in February and 53.8 ± 1.6 to 258.7 ± 7.3 dpm/L in April (Tables S1 and S2). The ^{224}Ra activity varies considerably in both the horizontal and vertical directions in the high salinity zone (Figure 2a). In the horizontal direction, the vertically averaged ^{224}Ra activity at each sampling site ranges from 106.1 to 172.8 dpm/L in February and 112.8 to 188.8 dpm/L in April. In the vertical direction, ^{224}Ra activity is generally lower at the shallow locations compared with the deeper locations. For example, ^{224}Ra activity at 0.5 m depth at sampling site S1 is 80.9 ± 2.0 and 71.7 ± 2.0 dpm/L in February and April, respectively, while the ^{224}Ra activity is twofold higher (164.9 ± 3.9 and 150.0 ± 4.7 dpm/L) at 2.0 m depth. The highest ^{224}Ra activity however was observed in the shallow aquifer at S3-2 (280.6 ± 6.4 and 258.7 ± 7.3 dpm/L in February and April, respectively; Tables S1 and S2). The dissolved Mn^{2+} concentrations were also considerably higher at S3-2 (0.22 and 0.14 mg/L in February and April) compared to deeper locations in the high salinity zone (e.g., S3-3 [0.080 and 0.077 mg/L] and S3-4 [0.047–0.070 mg/L], Liu, 2017), indicating that the high ^{224}Ra activity is caused by the reductive dissolution of Mn oxides releases adsorbed ^{224}Ra to the dissolved phase (Charette & Sholkovitz, 2006; Garcia-Orellana et al., 2014; Gonneea et al., 2008; Gonneea et al., 2013). ^{224}Ra activity in the nearshore seawater was relatively constant for the February and April sampling events (12.8 ± 0.3 and 11.6 ± 0.3 dpm/L, respectively).

### 3.2. ^{223}Ra

The spatial distribution of ^{223}Ra (Figure 2b) is similar to the ^{224}Ra distribution (Figure 2a) despite ^{223}Ra (actinium series) and ^{224}Ra (thorium series) belonging to different decay series. The spatial distribution of ^{223}Ra can be generalized as (1) ^{223}Ra activity in the freshwater groundwater zone is very low, (2) ^{223}Ra activity increases with salinity in the transition zone, and (3) ^{223}Ra activity is high in the high salinity zone with
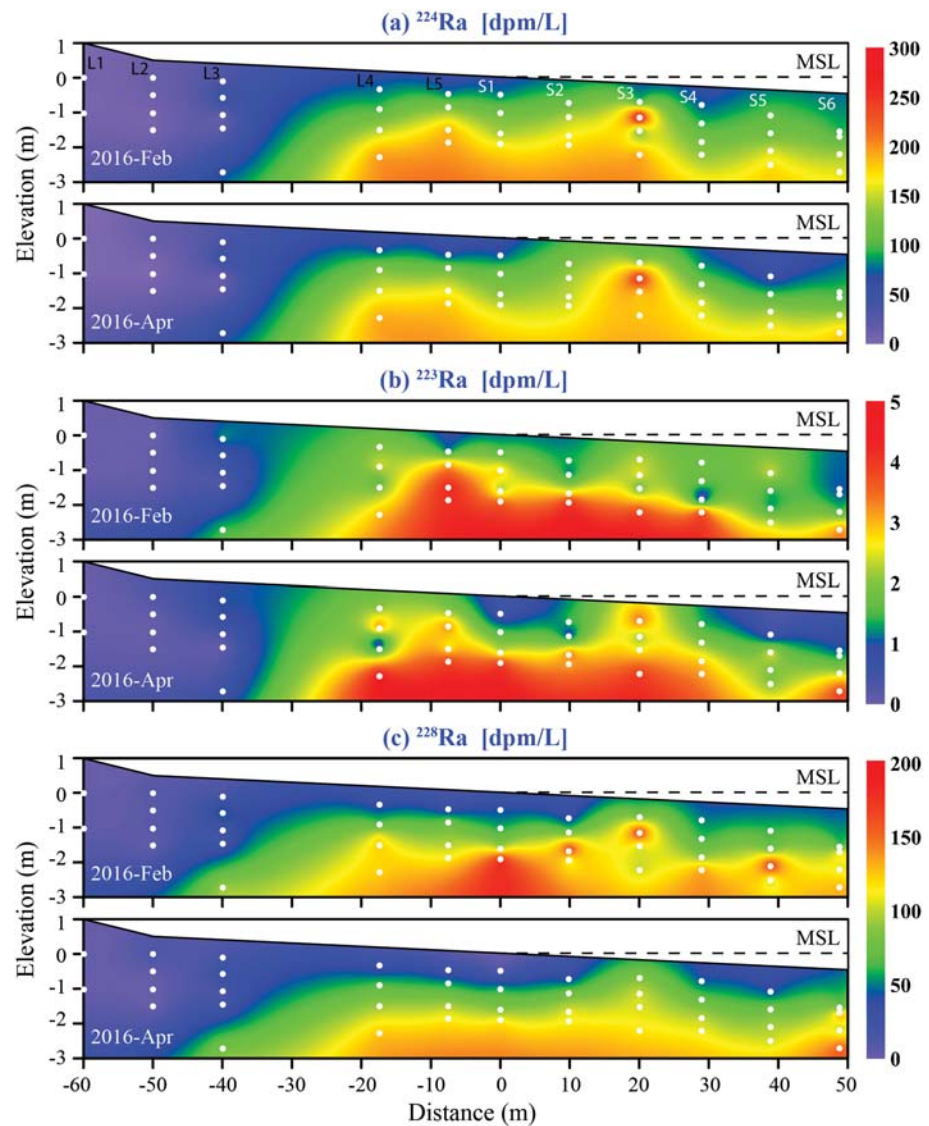
Figure 2. The spatial distributions of radium isotopes in nearshore aquifer in February and April 2016. (a) ^{224}Ra, (b) ^{223}Ra, and (c) ^{228}Ra.

higher activities at deeper locations compared to shallow locations. Specifically, in the fresh groundwater zone, ^{223}Ra activity varied from 0.07 ± 0.02 to 0.11 ± 0.02 dpm/L and 0.01 ± 0.00 to 0.03 ± 0.00 dpm/L in February and April, respectively (Tables S1 and S2). Similar to ^{224}Ra, the ^{223}Ra activity in fresh groundwater is lower in April compared to February due to lower salinity in the fresh groundwater zone in April because of the high rainfall between these sampling times. In the transition zone, ^{223}Ra activity ranges from 0.07 ± 0.02 to 1.44 ± 0.03 dpm/L and 0.05 ± 0.01 to 1.00 ± 0.03 dpm/L in February and April, respectively. In the shallow area of the high salinity zone (depth of ~0.5 m), ^{223}Ra activity varies from 1.02 ± 0.06 to 2.36 ± 0.04 dpm/L and 0.51 ± 0.04 to 3.44 ± 0.11 dpm/L in February and April, respectively. The lower ^{223}Ra activity at shallow locations compared to deeper locations is thought to be due to tidal flushing, mixing, and shorter residence times associated with the shallow tide-induced seawater circulations (Robinson et al., 2007). For site S1 ^{223}Ra activity is twofold and sevenfold higher at 2.0 m than at 0.5 m depth in February and April, respectively (3.62 ± 0.09 vs. 1.63 ± 0.07 dpm/L and 0.55 ± 0.03 vs. 3.96 ± 0.11 dpm/L). Similar to ^{224}Ra, the ^{223}Ra activity in nearshore seawater was similar in February and April (0.16 ± 0.01 and 0.22 ± 0.01 dpm/L, respectively).
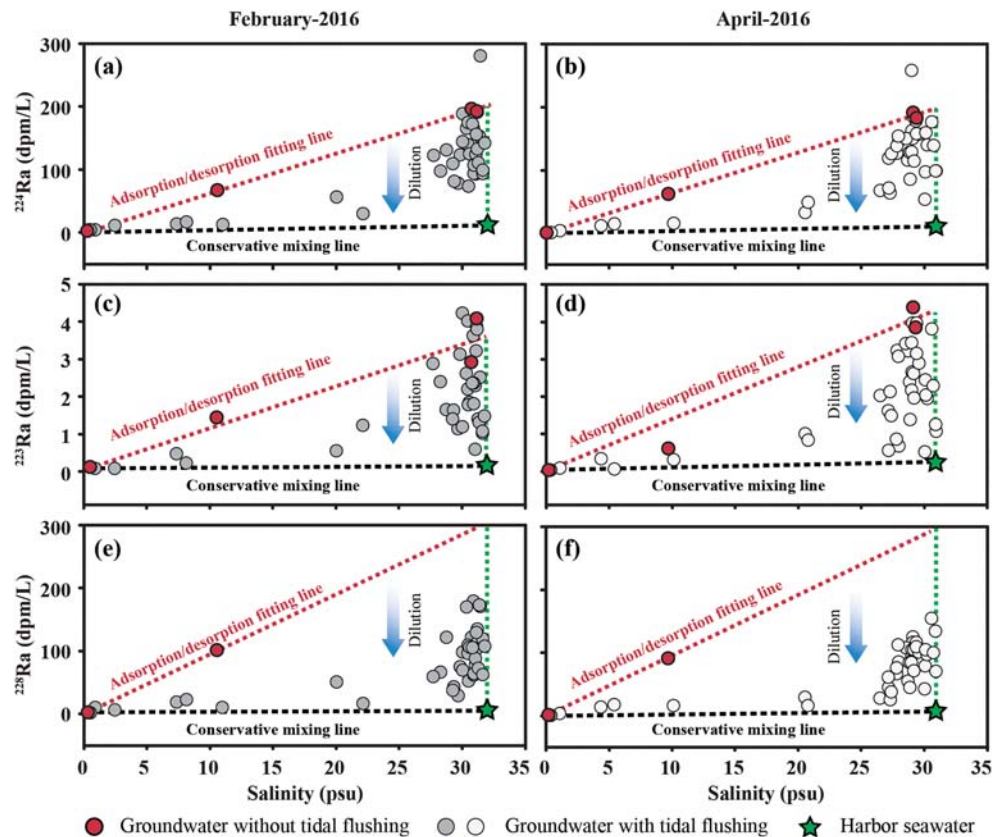
Figure 3. The correlations between salinity and radium isotopes in February and April 2016. ^{224}Ra versus salinity in (a) and (b), ^{223}Ra versus salinity in (c) and (d), and ^{228}Ra versus salinity in (e) and (f). The adsorption/desorption fitting line is made by linear fitting with points not affected by tidal flushing and mixing.

3.3. ^{228}Ra

^{228}Ra and ^{224}Ra belong to the same decay chain (^{232}Th decay chain). As a result, ^{228}Ra (Figure 2c) and ^{224}Ra (Figure 2a) have similar spatial distributions in the intertidal aquifer. In fresh groundwater, ^{228}Ra activity varied from 1.53 ± 0.11 to 2.63 ± 0.45 dpm/L and 0.24 ± 0.05 to 0.77 ± 0.09 dpm/L in February and April, respectively (Tables S1 and S2). In the transition zone, ^{228}Ra activity ranged from 5.94 ± 0.23 to 101.2 ± 3.7 dpm/L and 3.11 ± 0.22 to 91.2 ± 3.5 dpm/L in February and April, respectively. Similar to the ^{224}Ra, deeper groundwater in the transition zone (L3-5) had the highest ^{228}Ra activity. In the high salinity zone, ^{228}Ra activities ranged from 37.1 ± 0.9 to 178.7 ± 4.5 dpm/L in February and 27.61 ± 1.0 to 154.3 ± 5.7 dpm/L in April with the temporal and spatial variations of ^{228}Ra consistent with the variations in ^{224}Ra. Spatially, ^{228}Ra activity increased with the depth in the high salinity zone for both sampling events and consistent with temporal ^{224}Ra variations; ^{228}Ra activity at the deeper sampling locations is slightly lower in April compared to February (Figure 2c). ^{228}Ra activity in the nearshore seawater was similar in February and April (5.93 ± 0.15 and 6.02 ± 0.23 dpm/L, respectively).

4. Discussion

4.1. The Status of Radium Isotopes Equilibrium in the Intertidal Aquifer

When seawater enters the intertidal aquifer, the decay of thorium produces radium, and the radium decay occurs at the same time in the aquifer. The production rate generally surpasses the decay rate of radium isotopes due to the low activity of radium in seawater; therefore, the activity of radium isotopes would ingrowth as the residence time increases. As the ingrowth of radium occurs, the production rate becomes equal to the decay rate. At this point, the activity of radium does not increase further. This state is called the equilibrium of radium (Porcelli, 2008). Identification of the disequilibrium zone in the intertidal aquifer provides

valuable understanding of the flow dynamics, groundwater residence time, and the effects of tidal flushing and mixing. In the following sections, we use two methods to identify the equilibrium status of radium isotopes in the intertidal aquifer.

4.1.1. Ra and Salinity Relationship

Consistent with prior radium coastal groundwater studies (Charette et al., 2008; Kiro et al., 2014; Swarzenski, 2007; Webster et al., 1995), activities of the radium isotopes in the intertidal aquifer generally increase with salinity (Figure 3). This relationship is due to the desorption of radium isotopes from the sediment surface coatings as ionic strength increases. However, salinity is not the only factor that influences radium partitioning between the dissolved and solid phases. For instance, groundwater at L3-5 has a lower salinity but a higher Ra activity than that at L3-1. Factors such as grain size and surface area, and mineralogical sediment composition, dissolved Mn and Ba concentrations, and the pH and redox conditions generally also influence the radium partitioning (Beck & Cochran, 2013; Gonneea et al., 2008; Kiro et al., 2012). In this study, the shallow intertidal aquifer experiences frequent tidal flushing and mixing which may explain the decrease in the dissolved phase radium in this zone. Webster et al. (1995) derived a static model to describe the partitioning of radium isotopes considering the influence of salinity, the sediment/water ratio, and sediment adsorption properties, which can be expressed as

$$A_w = \left(R + \frac{a}{bS}\right)^{-1} A_0,$$

$$(2)$$

$$R = \frac{V_w}{V_s} = \frac{\varnothing}{1-\varnothing},$$

$$(3)$$

where A_w [dpm/L] is the dissolved radium isotope activity; A_0 [dpm/L] is the total exchangeable radium including the adsorbed (A_s) and dissolved (A_w) phases of radium isotopes, which can be expressed as $A_0 = \frac{\varnothing}{(1-\varnothing)}A_w + A_s$; R [—] is the ratio of the total water volume (V_w [L]) to sediment volume (V_s [L]); a and b are parameters that describe the degrees of attraction of radium and sodium ions to the sediment surface; and $\varnothing$ [—] is the porosity. Combining equations (2) and (3) leads to

$$\frac{A_0}{A_w} - \frac{\varnothing}{1-\varnothing} = \frac{a/b}{S}.$$

$$(4)$$

In this study, the measured $\varnothing$ is 0.3 (Liu, Jiao, & Cheng, 2018; Liu, Jiao, Liang, & Kuang, 2017). After substituting $\varnothing$ into equation (4), A_w can be expressed as a function of salinity, S [—],

$$A_w = \frac{1}{\frac{a/b}{S} + 0.43} A_0.$$

$$(5)$$

For our study site, S is small (ranges from 0 to 30), and a/b for typical sands (two types: grain sizes <63 μm and 125–500 μm) has a magnitude greater than 10,000 according to modeling results of Webster et al. (1995). Thus, $\frac{a/b}{S} \gg 0.43$ and equation (5) can be simplified to

$$A_w = \frac{A_0}{a/b} S.$$

$$(6)$$

According to equation (6), the activity of radium isotopes in the dissolved phase is a function of salinity. It should be noted that the laboratory experiment by Webster et al. (1995) was conducted under oxic conditions, which differs from the reducing environment of our study site. However, we do not expect the redox conditions to considerably influence the relationship described by equation (6) as both dissolved Mn and Ba concentrations, which are also influenced by the redox conditions and known to affect radium partitioning (Beck & Cochran, 2013; Gonneea et al., 2008; Kiro et al., 2012; Kiro et al., 2013), were very low in all sampling locations in the intertidal aquifer (Liu, 2017) except location S3-2. Therefore, although other factors generally have impact on radium partitioning, the salinity is thought to be the key factor controlling radium partitioning between the adsorbed and dissolved phases in this study.
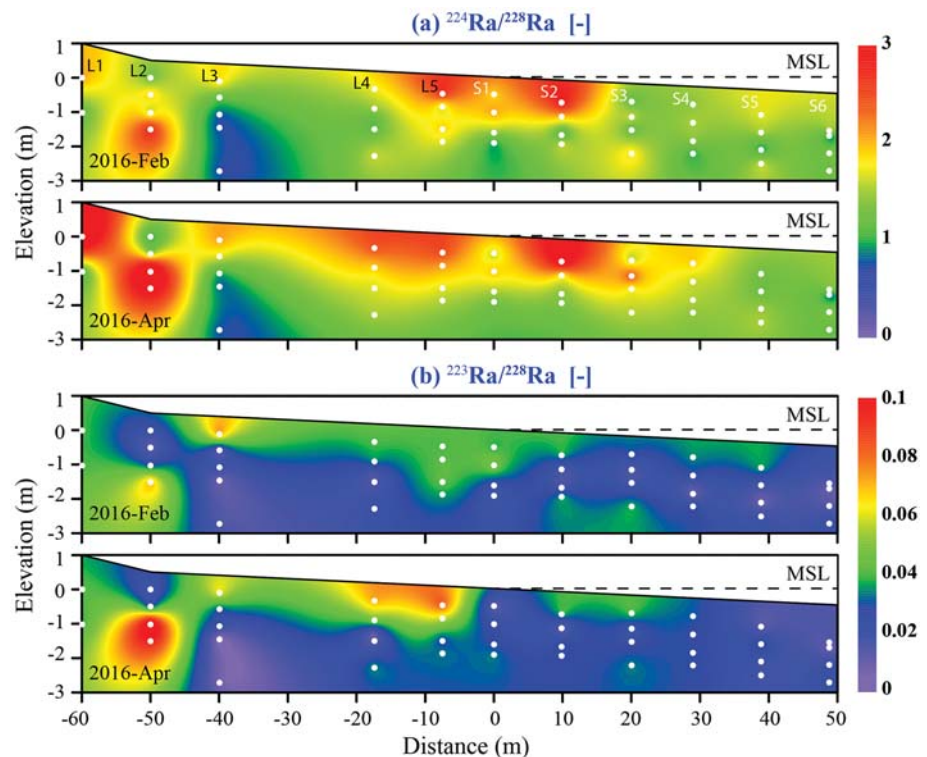
Table 1
The Measured Total Exchangeable ^{224}Ra in Bulk Sediments

ID	Depth (m)	Weight (g)	^{224}Ra activity (dpm/g)	Uncertainty (dpm/g)	Porosity[a] (—)	Dry density[a] (g/cm³)	A_0 (dpm/L)	Uncertainty (dpm/L)
1	0.34	19.85	0.67	0.04	0.3	2.7	1259	72.4
2	0.88	18.30	1.80	0.10	0.3	2.7	3409	189.2
3	1.00	19.27	2.18	0.11	0.3	2.7	4126	210.5

[a]The data are from Liu, Jiao, and Cheng (2018).

If the solid compositions and total exchangeable radium isotopes (A_0) in the intertidal aquifer are assumed to be homogeneous, $\frac{A_0}{a/b}$ is constant, and the radium activity has a linear relationship with salinity according to equation (6). However, measured total exchangeable ^{224}Ra activities for bulk sediment were found to be higher for the deeper sediments compared to the shallower intertidal sediments (Table 1). For example, the lower total exchangeable ^{224}Ra in the bulk sediment at a depth of 0.34 m (0.67 ± 0.04 dpm/g) is observed compared to that at a depth of 1.0 m (2.18 ± 0.11 dpm/g; Table 1). The lower total exchangeable radium in the shallow sediments is thought to be due to the continuous tidal flushing and mixing in the shallow sediments. It follows that for areas of the intertidal aquifer that are not influenced by tidal flushing and mixing (i.e., fresh groundwater zone and in the deep high salinity [salt-wedge] zone), the radium activities should be around the fitting line (called adsorption/desorption fitting line) described by equation (6). In contrast, for shallow areas affected by tidal flushing and mixing, the dissolved radium isotope activities are expected to be below the linear fitting line due to the lower production rate induced by depletion of total exchangeable radium.

Sampling points in the fresh groundwater zone and deep salt-wedge zone include L1-1, L1-2, L2-3, and L2-4 (fresh groundwater zone; $S < 1$), and L3-5 (deep salt-wedge zone, Liu, Jiao, Liang, & Luo, 2018). In Figure 3 it can be seen that the activity of radium isotopes for these sampling points fall on the theoretical absorption/desorption fitting line (equation (6); red line in Figures 3a–3d). This indicates that radium

Figure 4. The spatial distribution of the radium isotopic ratio of groundwater in the nearshore aquifer in February and April 2016. (a) ^{224}Ra/^{228}Ra and (b) ^{223}Ra/^{228}Ra.

Table 2
The Modeled Results Obtained From the Least Squares Fitting of Numerical Simulation and Measured Radium Distribution in the Intertidal Aquifer

Item	P_0 (dpm/L)	z_0 (m)	v (m/day)	K	RMSE	Equilibrium A_W (dpm/L)	$\tilde{x}$ (m)
[224]Ra	6.83×10^4	2.42	0.5	350	21.2	194.5	2.4
[223]Ra	8.91×10^2	1.15	0.5	350	0.84	2.53	1.2
[228]Ra	1.22×10^5	0.00	0.5	350	6.74	346.75	10.7

isotopes at these sampling points have reached equilibrium whereby the activity remains unchanged with increasing residence time. Measured radium activities that fall below the absorption/desorption line are in disequilibrium. It is worth noting that all [228]Ra activities in the high salinity zone are below the adsorption/desorption fitting line (Figures 3e and 3f), indicating that [228]Ra activities in this zone are in disequilibrium. The different behaviors of long-lived ([228]Ra) and short-lived ([224]Ra and [223]Ra) radium isotopes are because of the different [228]Ra and [224]Ra ingrowth rates in the aquifer. With a longer half-life, [228]Ra needs longer ingrowth time and characteristic distance along its flow paths to reach equilibrium (Porcelli, 2008). According to their spatial distributions (Figure 2), radium isotopes in the shallow (~upper 2 m) intertidal aquifer have not reached equilibrium (low activity of radium despite high salinity). Two possible reasons may explain this disequilibrium. First, intensive continuous tidal flushing over time leads to less total adsorbed radium isotopes in the shallow intertidal aquifer and subsequently less partitions onto the dissolved phase. Second, the dissolved radium isotopes in the shallow intertidal aquifer maybe diluted by newly infiltrating seawater with low radium activity.

4.1.2. [224]Ra/[228]Ra Ratios

[224]Ra and [228]Ra are both members of [232]Th decay series and closely related to each other. [232]Th produces [228]Ra through alpha decay while [228]Ra produces [228]Ac and then [228]Th (mother nuclide of [224]Ra) through beta decay. [224]Ra is subsequently produced through the alpha decay of [228]Th (Porcelli, 2008; Tricca et al., 2000; Tricca et al., 2001). When seawater infiltrates the intertidal aquifer on the rising tide, with the increase of residence time, the activity of both [224]Ra and [228]Ra will increase resulting in a stable [224]Ra/[228]Ra ratio until [224]Ra reaches equilibrium with respect to equal production and decay rates (Porcelli, 2008). Once it reaches equilibrium, the [224]Ra activity will be stable; however, [228]Ra ingrowth continues leading to a decreases in the [224]Ra/[228]Ra ratio until [228]Ra reaches equilibrium. After this, [224]Ra/[228]Ra ratio will be a constant value which is smaller than that before both [224]Ra and [228]Ra reach equilibrium state. Therefore, [224]Ra/[228]Ra ratio provides important insight into the equilibrium status of these radium isotopes as they are transported through the intertidal aquifer. In this study, [224]Ra/[228]Ra ranged from 0.66 to 2.95 in February and from 0.68 to 3.88 in April. The spatial distribution of [224]Ra/[228]Ra (Figure 4a) clearly shows that [224]Ra/[228]Ra decreases with depth in the high salinity zone in both February and April. For example, [224]Ra/[228]Ra varies from 1.21 to 2.95 in February (1.28 to 3.37 in April) in the shallow intertidal aquifer (depth of 0.5 m) while [224]Ra/[228]Ra varies from 0.92 to 1.87 in February (1.14 to 1.57 in April) deeper in the intertidal aquifer (depth of 2.5 m; Tables S1 and S2). The spatial distribution of [223]Ra/[228]Ra ratio is similar to the [224]Ra/[228]Ra ratio (Figure 4b). This is because both [223]Ra and [224]Ra are short-lived radium isotopes with high production rates compared with [228]Ra and therefore reach equilibrium faster. Therefore, the [224]Ra/[228]Ra and [223]Ra/[228]Ra ratios decrease with increasing groundwater residence time after [224]Ra and [223]Ra reach the equilibrium state. In this study, L3-5 located in the transition zone of the salt-wedge is thought to have a longer residence time than any other locations as explained previously. Consistent with this, the lowest [224]Ra/[228]Ra ratio was observed at L3-5 with values of 0.67 and 0.68 in February and April, respectively (Figure 4a and Tables 1 and 2). If both [224]Ra and [228]Ra have reached equilibrium state at L3-5, these ratio values represent the lower limit of the [224]Ra/[228]Ra ratio in the aquifer, and locations with larger [224]Ra/[228]Ra ratio are in disequilibrium state. Despite [224]Ra reaching equilibrium state at depth, as discussed in the previous section, [228]Ra takes longer to reach equilibrium state, and this is why [224]Ra/[228]Ra ratios (0.9 to1.6) at these locations where [224]Ra has reached the equilibrium state are much larger than [224]Ra/[228]Ra ratio (0.67) at L3-5 (Figure 4a and Tables S1 and S2). The disequilibrium status of Ra revealed through [224]Ra/[228]Ra ratio is consistent with that revealed through Ra versus salinity relationships in section 4.1.1.
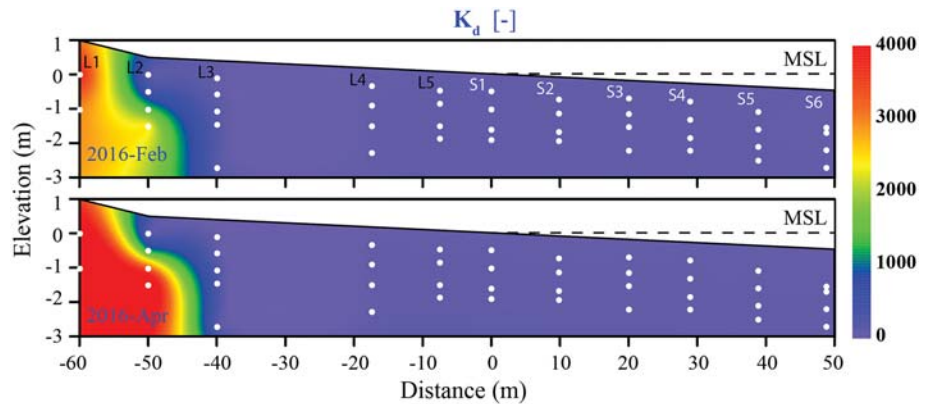
Figure 5. The spatial distribution of partitioning coefficient (K_d) of radium isotopes in the nearshore aquifer in February and April 2016.

4.2. Partitioning of Radium Isotopes

The radium distribution coefficient (K_d), defined as the ratio of adsorbed radium isotopes (A_s) and dissolved radium isotopes (A_w), can be expressed as

$$K_d = \frac{A_s}{A_w} = \frac{A_0 - \frac{\varnothing}{(1-\varnothing)}A_w}{A_w} = \frac{A_0}{A_w} - \frac{\varnothing}{(1-\varnothing)}. \tag{7}$$

Combining equations (7) and (4) gives

$$K_d = \frac{(a/b)}{S}, \tag{8}$$

a/b values determined by Webster et al. (1995) for sand with grain size <63 µm and sand with grain size 125–500 µm are used in our calculations to represent the upper and lower limit for our study site as >50% of sediments in the sandy aquifer have grain size <500 µm (Liu, Jiao, & Cheng, 2018). Adopting these values, equations (7) and (8) can be used to calculate the distribution coefficient (K_d) of radium isotopes, total exchangeable radium (A_0), and percentage of desorption at different salinities. The calculated results (Table S3) can be compared with A_0 calculated using the measured total exchangeable [224]Ra in bulk sediments at different depths (Table 1). For example, the calculated total exchangeable [224]Ra at L4-2 with a depth of 1.0 m is 3,109–5,526 dpm/L with an average value of 4,318 dpm/L (Table S3), and the measured total exchangeable [224]Ra in bulk sediments with a depth of 1.0 m near L4 is 4,126 ± 210.5 dpm/L (Table 1). Therefore, good comparison between the measured and calculated total exchangeable [224]Ra suggests that the approach used to calculate K_d and A_0 is valid.

The spatial distributions of K_d in February and April are presented in Figure 5. As expected, fresh groundwater has a large K_d value, whereas groundwater with high salinity has a small K_d value, meaning more radium isotopes partition to the solid phase in fresh groundwater than in high salinity groundwater (Kiro et al., 2014; Swarzenski, 2007; Webster et al., 1995). For example, average K_d value in fresh groundwater (L1-1, L1-2, and L2-4) ranges between 2,240 and 3,983, which is ~75 times the K_d values in the high salinity zone (30–53). In other words, <0.1% of radium isotopes exist in the dissolved phase in the fresh groundwater zone, and >1.7% of radium isotopes (1.7–3.5%) exist in the dissolved phase in the high salinity zone ($S > 25$; Table S3). As expected, K_d values decrease as the salinity increases in the transition zone. For instance, as the salinity increases from 0.9 at L2-3 to 11 at L2-1 (Table S1), K_d decreases from 1,405 to 114 in February (Table S3). The same relationship can also be observed in comparing the April and February radium isotope data. Due to the comparatively high precipitation in April, K_d values are higher in April compared to February due to lower salinity causing a shift of radium isotopes from the dissolved to the adsorbed phase.
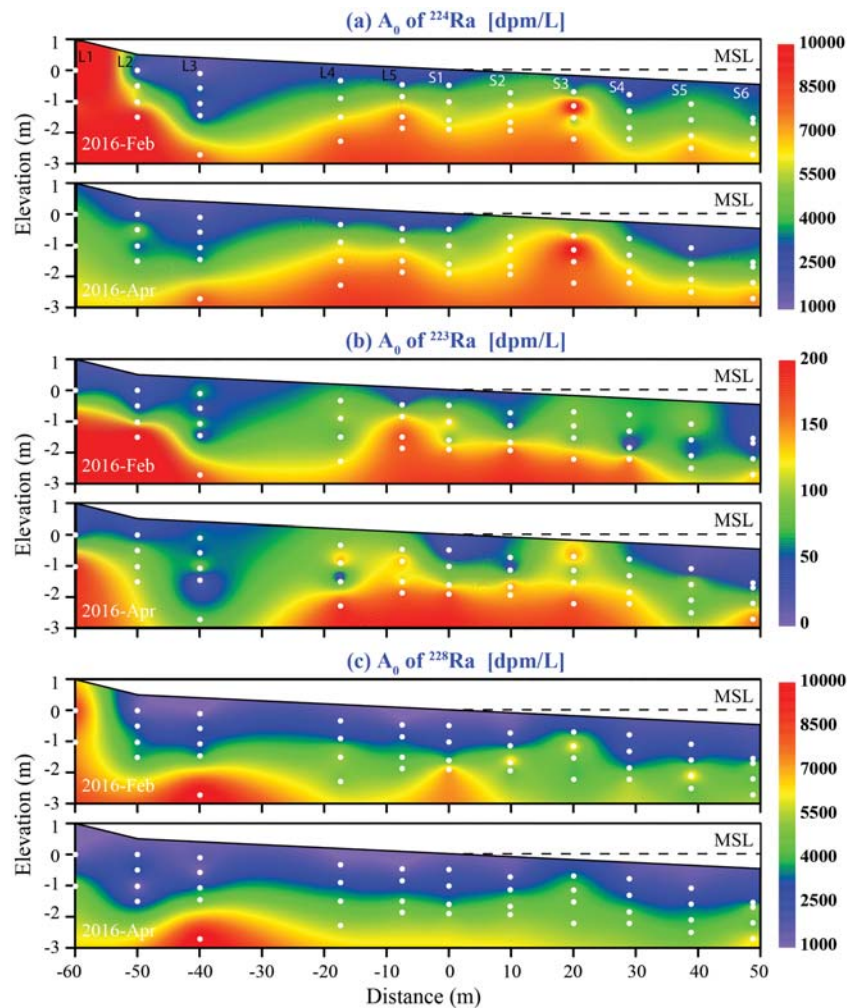
Figure 6. The total exchangeable radium isotopes (A_0) in February and April 2016. (a) ^{224}Ra, (b) ^{223}Ra, and (c) ^{228}Ra.

The spatial distribution of the total exchangeable radium isotopes (A_0) presented in Figure 6 clearly shows that the total exchangeable radium isotopes (^{224}Ra, ^{223}Ra, and ^{228}Ra) in the shallow intertidal aquifer are significantly lower than deeper in the aquifer in both February and April. For example, considering the total exchangeable ^{224}Ra in February (Figure 6a), ^{224}Ra ranges from 3,011 to 4,682 dpm/L with an average value of 3,744 dpm/L at a depth of ~0.5 m whereas it varies from 5,310 to 8,001 dpm/L with an average value of 6,979 dpm/L at a depth of 2.5 m (Table S3). The total exchangeable ^{224}Ra, ^{223}Ra, and ^{228}Ra in the shallow aquifer (depth of 0.5 m) are only 53.6% (53.4%), 48.5% (46.4%), and 42.2% (40.5%) of that deeper in the aquifer (depth of 2.5 m) in February (or April). The long-lived radium isotope, ^{228}Ra, has a higher percentage of activity loss between the deep and shallow aquifers due to smaller ingrowth rate compared to the short-lived radium isotopes (^{224}Ra and ^{223}Ra) in both February and April (Figure 6). This is consistent with ^{228}Ra needing a longer distance to reach the equilibrium state.

4.3. 1-D Reactive Transport Model for Radium Isotopes in the Intertidal Aquifer

In the high salinity zone of the intertidal aquifer, the transport of radium isotopes from the beach surface to the deep aquifer can assumed to be vertical as the low beach slope (1%) leads to negligible horizontal flow in the high salinity zone of this study. The ingrowth of radium in seawater infiltrating the intertidal aquifer is expected to be similar to the radium ingrowth in vertical water flow through wetland sediments as described by Krest and Harvey (2003). Assuming that the amount of adsorbed radium isotopes does not change with time (assuming the steady state of radium isotopes in the adsorbed phase, which means that the dissolved

radium isotopes adsorption is balanced by the adsorbed radium isotopes desorption and adsorbed radium isotopes decay) and the alpha recoil of mother nuclide on the surface coating has 100% efficiency to the dissolved phase (more details can be found in the Supporting Information; Luo et al., 2000; Porcelli, 2008), a one-dimensional model considering advection, dispersion, production, decay, and desorption/adsorption can be applied to simulate radium ingrowth along a flow line (Kiro et al., 2013).

$$\frac{\partial C}{\partial t} = -v\frac{dC}{dz} + D\frac{\partial^2 C}{\partial z^2} - \lambda(K+1)C + P, \tag{9}$$

where C [dpm/L] is the dissolved activity of radium isotopes; t [day] is the time; v [m/day] is the infiltration velocity, which is assumed to be uniform in a shallow aquifer; D [m^2/day] is the hydrodynamic dispersion coefficient; λ [1/day] is the decay constant of radium isotopes; K [—] is the dimensionless adsorption partition coefficient given as $K = [\rho_s/\varnothing] \times K_d$; and P [dpm/L/day] is the production rate of radium isotopes by alpha recoil, decay of mother nuclide on surface coatings and in the dissolved phase, and net desorption from surface coating (desorption − adsorption). In previous studies the production rate (P) has been assumed to be uniform across the nearshore aquifer with depth and does not change with time (Cai et al., 2014; Cai et al., 2015; Krest & Harvey, 2003). However, the vertical distribution of dissolved ^{228}Th is similar to its daughter nuclide (^{224}Ra) with lower activity in the shallow aquifer compared to the deeper aquifer due to shorter residence times. Even if we assume that tidal flushing does not affect the adsorbed phase of ^{228}Th as it has a much stronger affinity to the sediments than Ra isotopes, the total exchangeable ^{228}Th is still expected to be greater deeper in the aquifer than in the shallow sediments due to the ingrowth of ^{228}Th from ^{228}Ra. Therefore, the production rate of radium isotopes increases with depth. To account for this, we used an exponential relationship to describe the production rate (P) as a function of depth (z), which can be expressed as

$$P = P_0\left(1 - e^{-\beta\frac{z}{z_0}}\right), \tag{10}$$

where P_0 [dpm/L/day] is the production rate when radium isotopes are in equilibrium state, z_0 [m] is the characteristic depth where the production rate reaches 90% equilibrium production rate (Porcelli, 2008), z [m] is the depth, β is a fitting parameter ($\beta = \ln(10)$). β is calculated via equation (10) according to the definition of z_0 when assuming P is equal to 90% P_0 at $z = z_0$. As tidal fluctuations affect the radium dynamics in the intertidal aquifer, radium transport is a transient process, and theoretically, the steady state is not obtained. However, to improve our understanding of the ingrowth of radium isotopes in the intertidal aquifer, here we have assumed the radium distribution under steady phase-averaged hydrodynamic conditions with $\partial C/\partial t = 0$ (the dissolved phase of radium isotopes is in steady state). Moreover, due to high advection of seawater into the aquifer on the rising tide, the dispersion term is neglected. Using these assumptions, equation (9) is rewritten as

$$v\frac{dC}{dz} = -\lambda(K+1)C + P_0\left(1 - e^{-\beta\frac{z}{z_0}}\right). \tag{11}$$

The general solution of equation (11) is as follows with details on how to solve this equation provided in the Supporting Information,

$$C(z) = \left(C' - \frac{P_0}{\lambda(K+1)} + \frac{P_0 z_0}{\lambda(K+1)z_0 - \beta v}\right) \cdot e^{-\frac{\lambda(K+1)z}{v}} - \frac{P_0 z_0}{\lambda(K+1)z_0 - \beta v}e^{-\beta\frac{z}{z_0}} + \frac{P_0}{\lambda(K+1)}, \tag{12}$$

where C [dpm/L] is the activity of radium isotopes at the upper boundary. Here we have set C as the radium activity of harbor seawater.

This model was applied to sampling sites with similar salinity and pH (L4, L5, and S1 to S6) because K is affected by changes in salinity and pH (Beck & Cochran, 2013; Gonneea et al., 2008). According to Tables S1 and S2, salinity changes at L4 to L6 are within 2, and pH variation is small. In addition, the variation of calculated K_d values listed in Table S3 for these sampling sites is less than 4%. The best fit modeling results (least squares fitting method) are shown in Figure 7 with the parameters used in the best fit model
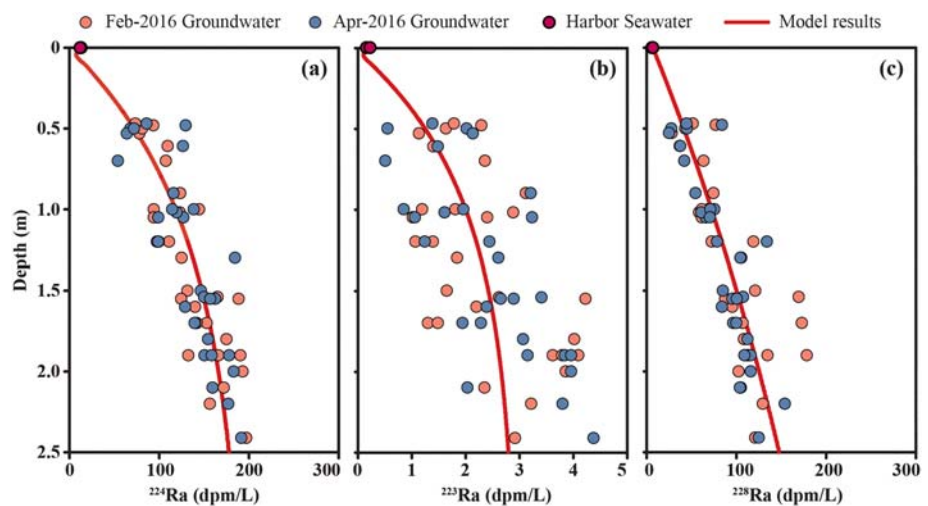
Figure 7. The vertical distribution of radium isotopes in the high salinity zone and reactive transport modeling results. (a) ^{224}Ra, (b) ^{223}Ra, and (c) ^{228}Ra.

provided in Table 2. Model sensitivity analysis to evaluate the effect of variations in the parameter values is presented in the Supporting Information.

The production rates (P_0) for the best model fit are 6.83×10^4, 8.91×10^2, and 1.22×10^5 dpm/L fluid for ^{224}Ra, ^{223}Ra, and ^{228}Ra, respectively. The P_0 for all radium isotopes are significantly larger than values available in the literature (Michael et al., 2011) with the P_0 for ^{223}Ra over one order of magnitude greater than literature values (i.e., 58 dpm/L fluid for Webster et al., 1994 and 44 dpm/L fluid for Rama & Moore, 1996). The K value which provided the best model fit is 350 with this value kept constant in matching the ^{224}Ra, ^{223}Ra, and ^{228}Ra data. The modeled K value is well within the range of K previously reported for saline environments (Beck & Cochran, 2013; Kiro et al., 2015; Webster et al., 1995). Importantly, the modeled K value is also within the range of our calculated values (202–365) from the adsorption/desorption static model (equation (8)). As can be seen in Table S3, K_d calculated via equation (8) for the radium isotopes at our study site ranges from 32 to 58, which corresponds to a K value between 202 and 365 for sampling locations not affected by the tidal flushing and mixing. In addition, according to the measured total exchangeable ^{224}Ra in bulk sediment (4,126 $\pm$ 210.5 dpm/L), the K at a depth of 1.0 m near L4 is calculated to be 266 in February and 205 in April. The limiting value of equation (12) is $P_0/(1+K)\lambda$, which represents the equilibrium activity of radium isotopes. The calculated equilibrium values of ^{224}Ra, ^{223}Ra, and ^{228}Ra are 194.5, 2.54, and 346.8 dpm/L, respectively. Assuming that the equilibrium state of ^{224}Ra and secular equilibrium (90% equilibrium) of ^{228}Ra are obtained at some locations in the aquifer, the theoretical ^{224}Ra/^{228}Ra ratio should be 0.62. This value is similar to the ^{224}Ra/^{228}Ra ratio of groundwater at L3-5 (0.66 and 0.68 in February and April, respectively, in Tables S1 and S2), supporting our previous analysis that L3-5 has the longest residence time and ^{224}Ra is in equilibrium state whereas ^{228}Ra is in secular equilibrium state at this location.

The vertical seepage velocity (v) that provided the simulated best match with the field data was 0.5 m/day (equivalent to 0.15 m/day Darcy velocity). The magnitude of this velocity is reasonable as it is similar to seepage velocity values previously reported for tide-induced infiltration, such as 0.18 m/day in Tricca et al. (2001), 0.1 m/day in Michael et al. (2011), and 0.027 to 0.27 m/day in Kiro et al. (2013). The modeled depths to reach the 90% equilibrium production rate (90% of P_0), that is, characteristic depth z_0 (Porcelli, 2008), for mother nuclides of ^{224}Ra, ^{223}Ra, and ^{228}Ra are 2.42, 1.15, and 0.00 m, respectively. The z_0 of mother nuclide for ^{228}Ra (^{232}Th, $t_{1/2}$ = 14.1 Gy) is much smaller than the other two mother nuclides (^{228}Th, $t_{1/2}$ = 1.9 years and ^{227}Th, $t_{1/2}$ = 18.7 days) for the short-lived radium isotopes (^{224}Ra and ^{223}Ra), which results from nearly conservative behavior of ^{232}Th in the intertidal aquifer due to its extremely long half-life. The characteristic depth ($\widetilde{x}$), defined as the depth where the activity of radium isotopes reaches 90% of secular equilibrium activity ($P_0/(1+K)\lambda$; Michael et al., 2011; Porcelli, 2008), can be calculated from $C(\widetilde{x}) = 90\% \, P_0/(1+K)\lambda$.

AGU
100
ADVANCING EARTH
AND SPACE SCIENCE

Water Resources Research

10.1029/2019WR024849

Table 3
Comparison of Dissolved ^{224}Ra and ^{228}Ra Concentrations in Coastal Groundwater in Prior Literature Studies

Water type	n	Salinity (—)	^{224}Ra (dpm/L)	^{228}Ra (dpm/L)	Location	Data source
Fresh groundwater	7	<1	0.82 ± 0.03–4.69 ± 0.20	0.24 ± 0.05–2.63 ± 0.45	Tolo Harbor, HK	This study
	9	<1	0.023 ± 0.004–0.16 ± 0.03	0.024 ± 0.004–0.19 ± 0.04	Long Island, NY	Tricca et al. (2001)
	34	0.18	0.11 ± 0.11	0.15 ± 0.14	Waquoit Bay, MA	Michael et al. (2011)
	1	<1	0.78 ± 0.08	N/A	Dead Sea, Israel	Kiro et al. (2012)
	9	<1	0.4–4.5	0.3–8.6	Dead Sea, Jordan	Kiro et al. (2015)
Saline groundwater	62	27.3–31.8	63.9 ± 1.8–280.6 ± 6.4	25.2 ± 0.88–178.7 ± 4.64	Tolo Harbor, HK	This study
	40, 16	All ranges	4.94 ± 2.02	1.96 ± 0.61	Jamaica Bay, NY	Beck et al. (2007)
	40	11.4–30.1	1.3 ± 0.4–15.4 ± 11	0.64 ± 0.07–7.41 ± 4.3	Waquoit Bay, MA	Michael et al. (2011)
	9	19.8–29.9	2.1 ± 0.1–19.2 ± 0.5	N/A	Yeoja Bay, Korea	Lee et al. (2010)
	9	16.1–32.5	3.56–16.15	2.22–7.84	Wadden Sea, Germany	Moore et al. (2011)
	2	11.3–19	1.74–2.03	11.34 ± 0.12–1.73 ± 0.15	Tampa Bay, USA	Swarzenski et al. (2007)
	2	5–15	0.63–5.71	5.42	Barataria Bay, USA	Moore and Krest (2004)
	19	22.35–32.92	4.87 ± 0.49–90.69 ± 9.1	N/A	Daya Bay, China	Wang et al. (2018)
	13	12.3–50.3	4.39 ± 0.31–40.1 ± 2.8	0.92 ± 0.06–6.51 ± 0.46	Jiaozhou Bay, China	Zhang et al. (2017)
	48	25–150	2.0–108.3	0.3–38	Dead Sea	Kiro et al. (2015)

Note. The activity of ^{224}Ra and ^{228}Ra is the average value.

Specifically, the characteristic depth for ^{224}Ra, ^{223}Ra, and ^{228}Ra in this study is 2.4, 1.2, and 10.7 m, respectively.

4.4. High Dissolved Radium Isotopes in Groundwater and Their Origins

Overall, our study site has high activities of ^{224}Ra and ^{228}Ra compared to other coastal aquifers. The activity of both ^{224}Ra and ^{228}Ra in fresh groundwater is much higher than previous studies (Kiro et al., 2012; Michael et al., 2011; Tricca et al., 2001) with the exception of a study site in the Dead Sea, Jordan (Kiro et al., 2015; Table 3). In saline groundwater, the ^{224}Ra and ^{228}Ra are also higher in this study than reported previously (Beck et al., 2007; Kiro et al., 2015; Lee et al., 2010; Michael et al., 2011; Moore et al., 2011; Moore & Krest, 2004; Swarzenski, 2007). The high production rate (P_0) and low dimensionless adsorption partition coefficient (K) lead to the high ^{224}Ra activity at our study site. Based on the model results, P_0 at our study site (6.83×10^4 dpm/L fluid) is greater than reported in the literature (Michael et al., 2011). Moreover, K at our study site (calculated value: 202–365; measured value: 266 in February and 205 in April; modeled value: 350) is smaller than reported previously, for example, 4,800 in Krishnaswami et al. (1982), 2,180–4,940 in Gonneea et al. (2008), and 940 in Michael et al. (2011), indicating that a higher proportion of radium isotopes exist in the dissolved phase at our study site compared to previous study sites. The high ^{228}Ra at our study site is also due to low K and high P_0 that are approximately two orders of magnitude greater than previous studies (Michael et al., 2011; Rama & Moore, 1996; Webster et al., 1994).

As mentioned previously, the production rate considers alpha recoil from the solid grain lattice, the decay of the parent nuclide on the sediment surface coatings, the decay of the dissolved parent nuclide, and net desorption from surface coatings (Porcelli, 2008; Tricca et al., 2001). For example, considering ^{224}Ra, the production could be (1) the decay of ^{228}Th in the sediment grain lattice via alpha recoil, (2) the decay of adsorbed ^{228}Th on sediment surface coating, (3) the decay of dissolved ^{228}Th, and (4) net desorption of ^{224}Ra from sediment surface coatings (Porcelli, 2008; Tricca et al., 2001). The decay of high-activity ^{228}Ra observed in this study would produce high activity of total exchangeable (adsorbed and dissolved) ^{228}Th through beta decay. Since ^{228}Th has a half-life of 1.91 years, the weathering input is usually neglected (Porcelli, 2008); therefore, all total exchangeable ^{228}Th is from the beta decay of ^{228}Ra. Afterwards, through alpha decay of exchangeable ^{228}Th produced from ^{228}Ra, high activity of total exchangeable ^{224}Ra will be obtained. According to the ^{224}Ra/^{228}Ra ratios in Tables S1 and S2, the dissolved ^{228}Ra at the majority of the sampling locations can support more than 60% of the dissolved ^{224}Ra. In addition, the adsorbed phase of ^{228}Ra would also contribute to the dissolved ^{224}Ra. In this case, the total exchangeable ^{228}Ra can support high-activity dissolved ^{224}Ra, and alpha recoil from grain lattice has minor contribution to the high-activity dissolved ^{224}Ra. Therefore, the high-activity ^{224}Ra and ^{228}Ra in this study are ascribed to the decay of parent
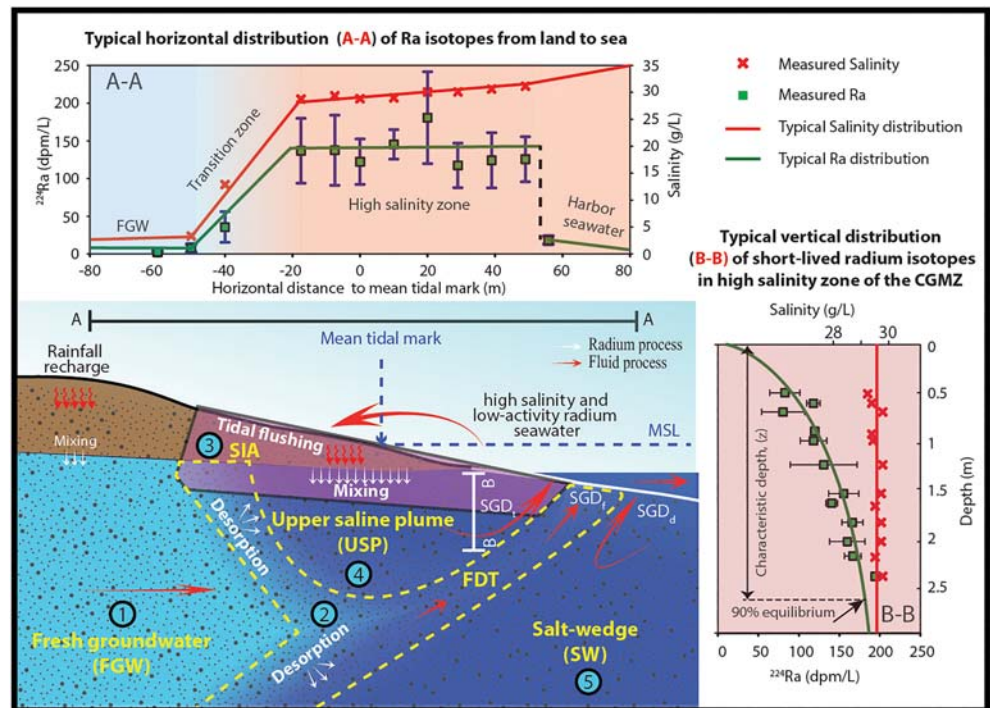
Figure 8. Conceptual diagram illustrating radium isotope processes in the intertidal aquifer. The red arrows represent the flow processes, and the white arrows depict the main radium processes in the intertidal aquifer. Fresh groundwater (FGW), upper saline plume (USP) driven by tidal fluctuation, freshwater discharge tube (FDT) driven by land-sea hydraulic gradient, and salt-wedge (SW) driven by density differences are identified (Robinson et al., 2007) according to the flow process while zones ① to ⑤ are identified according to the controlling process of radium. The measured data are taken from Tables S1 and S2 (salinity and ^{224}Ra). For A-A, the average value of salinity and ^{224}Ra at each sampling site is used, and for B-B, the average value is calculated from the data taken at the same depth in the high salinity zone. The 90% equilibrium is obtained according to the vertical infiltration model.

nuclide (Th) on the surface coating of solid grains. This is because ^{228}Th and ^{232}Th, the parent nuclides of ^{224}Ra and ^{228}Ra, have a very low solubility and strong sorption (Porcelli & Swarzenski, 2003; Tricca et al., 2001).

4.5. Implications for Coastal Groundwater Endmember Selection

Based on our field data and analysis, the general distribution of radium isotopes in an intertidal aquifer is conceptualized in Figure 8. In the transition zone where the freshwater mixes with the seawater, the radium activity increases due to redistribution of radium between the adsorbed and dissolved phases. Once the high-radium saline groundwater flows across the aquifer-sea interface, the radium activity drops rapidly due to the dilution with the low-activity seawater. The activity of radium isotopes in seawater continues to decrease with increasing distance from the shore due to offshore mixing processes (Moore, 2000). The vertical activity of the radium isotopes in the high salinity zone of the intertidal aquifer increases exponentially with the depth due to increasing residence time of the infiltrating seawater and radium ingrowth in the aquifer (Krest & Harvey, 2003; Porcelli, 2008). The activity of radium isotopes in the infiltrating seawater increases over a characteristic vertical distance, $\tilde{x}$, after which it reaches equilibrium with respect to its partitioning between the dissolved and solid phases, and then remains constant (Tricca et al., 2001). Note that this general conceptualization of radium behavior in the intertidal aquifer does not consider transient hydrodynamic forcing, aquifer heterogeneity, preferential flow paths, coprecipitation with other minerals, and bioturbation which will alter groundwater flow patterns and the salinity distribution.

Consistent with the findings of Michael et al. (2011), our data and analysis indicate that it may not be possible to select one endmember to represent all SGD fluxes driven by different forces due to the high spatial variability of radium isotopes in the intertidal aquifer. Generally, the driving force of SGD with shorter time scale

has a shorter and shallower flow path in the aquifer (Michael et al., 2011). For example, flows driven by density difference and seasonal perturbations generally have longer and deeper flow paths and affect a larger subsurface area in the nearshore aquifer than tide- and wave-driven flows. Therefore, SGD fluxes driven by different forces need to be estimated separately when using radium isotopes as a tracer with the respective endmembers chosen for the different SGD fluxes from different locations in the aquifer. In this case, the endmember for tide- and wave-driven SGD should be selected at a shallow location of the aquifer while seasonally driven or density-driven SGD endmember should correspond to a deeper location in the aquifer. In this study, based on the horizontal distribution of radium isotopes, it is evident that radium isotopes are less variable in the high salinity zone than the transition zone as the salinity variations are small. Vertically, the radium activity in the shallow intertidal aquifer is in disequilibrium due to the short residence time and effects of tidal flushing and mixing. In addition, as most tide-induced circulations discussed in this study follow shallow flow paths (Liu, Jiao, & Cheng, 2018), the endmember for calculating SGD volumes for shallow seawater circulations through the intertidal zone (tide- and wave-driven SGD) should be selected using samples collected at a depth less than the depth radium activity reaches equilibrium. For those SGDs with longer time scale and deep flow path such as seasonally driven and density-driven SGD, the endmember should be selected in the equilibrium zone of Ra. Using this approach will reduce the uncertainty in estimating tide-driven SGD compared to the traditional method of selecting the groundwater endmember based on groundwater samples randomly collected in the coastal aquifer (Lee, 2012). Importantly, to be able to select groundwater endmembers based on the SGD component requires the fact that SGD fluxes are estimated separately according to their driving forces. Estimating SGD components according to their driving forces can be done by applying multiple radium isotopes. By solving the mass balance of each radium isotopes, the unknown SGDs driven by different forces can be obtained. In addition, due to the complexity of the intertidal aquifer system, it is recommended that the overall flow patterns and geochemical distribution (salinity, temperature, or radium isotopes) in the intertidal aquifer are evaluated before selecting a suitable groundwater endmember.

5. Conclusions

This study provides a high-resolution two-dimensional spatial distribution of radium isotopes in an intertidal aquifer covering all the different zones in the aquifer (fresh groundwater zone, transition zone, and high salinity zone). The behavior of radium isotopes in the intertidal aquifer is affected by sharp salinity gradients, as well as tidal flushing and mixing through the shallow intertidal sediments. The field data reveal that radium isotopes in the shallow intertidal sediments are in disequilibrium because of tidal flushing, dilution with recirculating seawater, and short residence times. This disequilibrium affects the vertical distribution of dissolved radium isotopes (^{224}Ra, ^{223}Ra, and ^{228}Ra). A new one-dimensional diagenetic reactive transport model that considers depth-dependent production rates successfully simulated the vertical transport of radium isotopes in the intertidal aquifer. Based on least squares fitting the model results to the field data, the production rates of ^{224}Ra, ^{223}Ra, and ^{228}Ra are estimated to be 6.83×10^4, 8.91×10^2, and 1.22×10^5 dpm/L fluid, respectively, with the characteristic depths for ^{224}Ra, ^{223}Ra, and ^{228}Ra to reach 90% of equilibrium determined to be 2.4, 1.2, and 10.7 m, respectively. The modeled dimensionless adsorption partition coefficient K was determined to be 350 in the intertidal aquifer, which agrees well with values calculated using an adsorption/desorption model (202–365) and also to measured values (266 in February and 205 in April). The activity of radium isotopes in our study is higher than previous studies which is thought to be due to higher production rates and a lower partitioning coefficient. The distribution of radium isotopes in the intertidal aquifer shown in this study provides important information needed for selecting representative groundwater endmembers in SGD estimations. Based on combined analysis of the flow patterns and radium isotope distributions, the endmember for tide- and wave-driven SGD with shallow flow path should be selected in the disequilibrium zone of Ra while the endmember for seasonally driven and density-driven SGD with deep flow path should be selected in the equilibrium zone of Ra.

References

Abarca, E., Karam, H., Hemond, H. F., & Harvey, C. F. (2013). Transient groundwater dynamics in a coastal aquifer: The effects of tides, the lunar cycle, and the beach profile. *Water Resources Research*, *49*, 2473–2488. https://doi.org/10.1002/wrcr.20075

Beck, A. J., & Cochran, M. A. (2013). Controls on solid-solution partitioning of radium in saturated marine sands. *Marine Chemistry*, *156*, 38–48. https://doi.org/10.1016/j.marchem.2013.01.008

Beck, A. J., Rapaglia, J. P., Cochran, J. K., & Bokuniewicz, H. J. (2007). Radium mass-balance in Jamaica Bay, NY: Evidence for a substantial flux of submarine groundwater. *Marine Chemistry*, *106*(3-4), 419–441. https://doi.org/10.1016/j.marchem.2007.03.008

Burnett, W. C., Aggarwal, P. K., Aureli, A., Bokuniewicz, H., Cable, J. E., Charette, M. A., et al. (2006). Quantifying submarine groundwater discharge in the coastal zone via multiple methods. *Science of the Total Environment*, *367*(2-3), 498–543. https://doi.org/10.1016/j.scitotenv.2006.05.009

Cai, P., Shi, X., Hong, Q., Li, Q., Liu, L., Guo, X., & Dai, M. (2015). Using ^{224}Ra/^{228}Th disequilibrium to quantify benthic fluxes of dissolved inorganic carbon and nutrients into the Pearl River Estuary. *Geochimica et Cosmochimica Acta*, *170*, 188–203. https://doi.org/10.1016/j.gca.2015.08.015

Cai, P., Shi, X., Moore, W. S., & Dai, M. (2012). Measurement of ^{224}Ra:^{228}Th disequilibrium in coastal sediments using a delayed coincidence counter. *Marine Chemistry*, *138-139*, 1–6. https://doi.org/10.1016/j.marchem.2012.05.004

Cai, P., Shi, X., Moore, W. S., Peng, S., Wang, G., & Dai, M. (2014). ^{224}Ra:^{228}Th disequilibrium in coastal sediments: Implications for solute transfer across the sediment–water interface. *Geochimica et Cosmochimica Acta*, *125*, 68–84. https://doi.org/10.1016/j.gca.2013.09.029

Cerdà-Domènech, M., Rodellas, V., Folch, A., & Garcia-Orellana, J. (2017). Constraining the temporal variations of Ra isotopes and Rn in the groundwater end-member: Implications for derived SGD estimates. *Science of the Total Environment*, *595*, 849–857. https://doi.org/10.1016/j.scitotenv.2017.03.005

Charette, M. A., & Buesseler, K. O. (2004). Submarine groundwater discharge of nutrients and copper to an urban subestuary of Chesapeake bay (Elizabeth River). *Limnology and Oceanography*, *49*(2), 376–385. https://doi.org/10.4319/lo.2004.49.2.0376

Charette, M. A., Moore, W. S., & Burnett, W. C. (2008). Chapter 5 Uranium- and thorium-series nuclides as tracers of submarine groundwater discharge. In S. Krishnaswami & J. K. Cochran (Eds.), *Radioactivity in the environment* (pp. 155-191). Oxford, UK: Elsevier.

Charette, M. A., & Sholkovitz, E. R. (2006). Trace element cycling in a subterranean estuary: Part 2. Geochemistry of the pore water. *Geochimica et Cosmochimica Acta*, *70*(4), 811–826. https://doi.org/10.1016/j.gca.2005.10.019

Cho, H. M., & Kim, G. (2016). Determining groundwater Ra end-member values for the estimation of the magnitude of submarine groundwater discharge using Ra isotope tracers. *Geophysical Research Letters*, *43*, 3865–3871. https://doi.org/10.1002/2016GL068805

Fetter, C. W. (2000). *Applied hydrogeology*. New Jersey: Prentice Hall.

Garcia-Orellana, J., Cochran, J. K., Bokuniewicz, H., Daniel, J. W. R., Rodellas, V., & Heilbrun, C. (2014). Evaluation of ^{224}Ra as a tracer for submarine groundwater discharge in Long Island Sound (NY). *Geochimica et Cosmochimica Acta*, *141*, 314–330. https://doi.org/10.1016/j.gca.2014.05.009

Garcia-Solsona, E., Garcia-Orellana, J., Masqué, P., & Dulaiova, H. (2008). Uncertainties associated with ^{223}Ra and ^{224}Ra measurements in water via a Delayed Coincidence Counter (RaDeCC). *Marine Chemistry*, *109*(3-4), 198–219. https://doi.org/10.1016/j.marchem.2007.11.006

Gonneea, M. E., & Charette, M. A. (2014). Hydrologic controls on nutrient cycling in an unconfined coastal aquifer. *Environmental Science & Technology*, *48*(24), 14,178–14,185. https://doi.org/10.1021/es503313t

Gonneea, M. E., Morris, P. J., Dulaiova, H., & Charette, M. A. (2008). New perspectives on radium behavior within a subterranean estuary. *Marine Chemistry*, *109*(3-4), 250–267. https://doi.org/10.1016/j.marchem.2007.12.002

Gonneea, M. E., Mulligan, A. E., & Charette, M. A. (2013). Seasonal cycles in radium and barium within a subterranean estuary: Implications for groundwater derived chemical fluxes to surface waters. *Geochimica et Cosmochimica Acta*, *119*, 164–177. https://doi.org/10.1016/j.gca.2013.05.034

Heiss, J. W., & Michael, H. A. (2014). Saltwater-freshwater mixing dynamics in a sandy beach aquifer over tidal, spring-neap, and seasonal cycles. *Water Resources Research*, *50*, 6747–6766. https://doi.org/10.1002/2014WR015574

Heiss, J. W., Post, V. E. A., Laattoe, T., Russoniello, C. J., & Michael, H. A. (2017). Physical controls on biogeochemical processes in intertidal zones of beach aquifers. *Water Resources Research*, *53*, 9225–9244. https://doi.org/10.1002/2017WR021110

Kiro, Y., Weinstein, Y., Starinsky, A., & Yechieli, Y. (2013). Groundwater ages and reaction rates during seawater circulation in the Dead Sea aquifer. *Geochimica et Cosmochimica Acta*, *122*, 17–35. https://doi.org/10.1016/j.gca.2013.08.005

Kiro, Y., Weinstein, Y., Starinsky, A., & Yechieli, Y. (2014). The extent of seawater circulation in the aquifer and its role in elemental mass balances: A lesson from the Dead Sea. *Earth and Planetary Science Letters*, *394*, 146–158. https://doi.org/10.1016/j.epsl.2014.03.010

Kiro, Y., Weinstein, Y., Starinsky, A., & Yechieli, Y. (2015). Application of radon and radium isotopes to groundwater flow dynamics: An example from the Dead Sea. *Chemical Geology*, *411*, 155–171. https://doi.org/10.1016/j.chemgeo.2015.06.014

Kiro, Y., Yechieli, Y., Voss, C. I., Starinsky, A., & Weinstein, Y. (2012). Modeling radium distribution in coastal aquifers during sea level changes: The Dead Sea case. *Geochimica et Cosmochimica Acta*, *88*, 237–254. https://doi.org/10.1016/j.gca.2012.03.022

Krest, J. M., & Harvey, J. W. (2003). Using natural distributions of short-lived radium isotopes to quantify groundwater discharge and recharge. *Limnology and Oceanography*, *48*(1), 290–298. https://doi.org/10.4319/lo.2003.48.1.0290

Krishnaswami, S., Graustein, W. C., Turekian, K. K., & Dowd, J. F. (1982). Radium, thorium and radioactive lead isotopes in groundwaters: Application to the in situ determination of adsorption-desorption rate constants and retardation factors. *Water Resources Research*, *18*(6), 1663–1675. https://doi.org/10.1029/WR018i006p01663

Lee, C. M. (2012). Estimation of submarine groundwater discharge and nutrient loading of Tolo Harbour. Mphil Thesis The University of Hong Kong.

Lee, C. M., Jiao, J. J., Luo, X., & Moore, W. S. (2012). Estimation of submarine groundwater discharge and associated nutrient fluxes in Tolo Harbour, Hong Kong. *Science of the Total Environment*, *433*, 427–433. https://doi.org/10.1016/j.scitotenv.2012.06.073

Lee, Y. W., Kim, G., Lim, W. A., & Hwang, D. W. (2010). A relationship between submarine groundwater-borne nutrients traced by Ra isotopes and the intensity of dinoflagellate red-tides occurring in the southern sea of Korea. *Limnology and Oceanography*, *55*(1), 1–10. https://doi.org/10.4319/lo.2010.55.1.0001

Li, L., Barry, D. A., Stagnitti, F., & Parlange, J. Y. (1999). Submarine groundwater discharge and associated chemical input to a coastal sea. *Water Resources Research*, *35*(11), 3253–3259. https://doi.org/10.1029/1999WR900189

Liu, Y. (2017). Geochemical processes and solute transport in coastal groundwater mixing zone. Ph. D Thesis, The University of Hong Kong.

Liu, Y., Jiao, J. J., & Cheng, H. K. (2018). Tracing submarine groundwater discharge flux in Tolo Harbor, Hong Kong (China). *Hydrogeology Journal*, *26*(6), 1857–1873. https://doi.org/10.1007/s10040-018-1736-z

Liu, Y., Jiao, J. J., & Liang, W. (2018). Tidal fluctuation influenced physicochemical parameter dynamics in coastal groundwater mixing zone. *Estuaries and Coasts*, *41*(4), 988–1001. https://doi.org/10.1007/s12237-017-0335-x

Liu, Y., Jiao, J. J., Liang, W., & Luo, X. (2017). Tidal pumping-induced nutrients dynamics and biogeochemical implications in an intertidal aquifer. *Journal of Geophysical Research: Biogeosciences*, *122*, 3322–3342. https://doi.org/10.1002/2017JG004017

Liu, Y., Jiao, J. J., Liang, W., & Luo, X. (2018). Using tidal fluctuation-induced dynamics of radium isotopes (^{224}Ra, ^{223}Ra, and ^{228}Ra) to trace the hydrodynamics and geochemical reactions in a coastal groundwater mixing zone. *Water Resources Research*, *54*, 2909–2930. https://doi.org/10.1002/2017WR022456

Liu, Y., Jiao, J. J., Liang, W. Z., & Kuang, X. X. (2017). Hydrogeochemical characteristics in coastal groundwater mixing zone. *Applied Geochemistry*, *85*, 49–60. https://doi.org/10.1016/j.apgeochem.2017.09.002

Liu, Y., Jiao, J. J., & Luo, X. (2016). Effects of inland water level oscillation on groundwater dynamics and land-sourced solute transport in a coastal aquifer. *Coastal Engineering*, *114*, 347–360. https://doi.org/10.1016/j.coastaleng.2016.04.021

Liu, Y., Liang, W., & Jiao, J. J. (2018). Seasonality of nutrient flux and biogeochemistry in an intertidal aquifer. *Journal of Geophysical Research: Oceans*, *123*, 6116–6135. https://doi.org/10.1029/2018JC014197

Liu, Y., Not, C., Jiao, J. J., Liang, W., & Lu, M. (2019). Tidal induced dynamics and geochemical reactions of trace metals (Fe, Mn, and Sr) in the salinity transition zone of an intertidal aquifer. *Science of the Total Environment*, *664*, 1133–1149. https://doi.org/10.1016/j.scitotenv.2019.01.374

Luo, S. D., Ku, T. L., Roback, R., Murrell, M., & McLing, T. L. (2000). In-situ radionuclide transport and preferential groundwater flows at INEEL (Idaho): Decay-series disequilibrium studies. *Geochimica et Cosmochimica Acta*, *64*(5), 867–881. https://doi.org/10.1016/S0016-7037(99)00373-7

Luo, X., Jiao, J. J., Moore, W. S., & Lee, C. M. (2014). Submarine groundwater discharge estimation in an urbanized embayment in Hong Kong via short-lived radium isotopes and its implication of nutrient loadings and primary production. *Marine Pollution Bulletin*, *82*(1-2), 144–154. https://doi.org/10.1016/j.marpolbul.2014.03.005

Luo, X., Kwok, K. L., Liu, Y., & Jiao, J. (2017). A permanent multilevel monitoring and sampling system in the coastal groundwater mixing zones. *Ground Water*, *55*(4), 577–587. https://doi.org/10.1111/gwat.12510

McAllister, S. M., Barnett, J. M., Heiss, J. W., Findlay, A. J., MacDonald, D. J., Dow, C. L., et al. (2015). Dynamic hydrologic and biogeo-chemical processes drive microbially enhanced iron and sulfur cycling within the intertidal mixing zone of a beach aquifer. *Limnology and Oceanography*, *60*(1), 329–345. https://doi.org/10.1002/lno.10029

Michael, H. A., Charette, M. A., & Harvey, C. F. (2011). Patterns and variability of groundwater flow and radium activity at the coast: A case study from Waquoit Bay, Massachusetts. *Marine Chemistry*, *127*(1-4), 100–114. https://doi.org/10.1016/j.marchem.2011.08.001

Moore, W. S. (1996). Large groundwater inputs to coastal waters revealed by ^{226}Ra enrichments. *Nature*, *380*(6575), 612–614. https://doi.org/10.1038/380612a0

Moore, W. S. (1999). The subterranean estuary: A reaction zone of ground water and sea water. *Marine Chemistry*, *65*(1-2), 111–125. https://doi.org/10.1016/S0304-4203(99)00014-6

Moore, W. S. (2000). Determining coastal mixing rates using radium isotopes. *Continental Shelf Research*, *20*(15), 1993–2007. https://doi.org/10.1016/S0278-4343(00)00054-6

Moore, W. S. (2008). Fifteen years experience in measuring ^{224}Ra and ^{223}Ra by delayed-coincidence counting. *Marine Chemistry*, *109*(3-4), 188–197. https://doi.org/10.1016/j.marchem.2007.06.015

Moore, W. S. (2010). The effect of submarine groundwater discharge on the ocean. *Annual Review of Marine Science*, *2*(1), 59–88. https://doi.org/10.1146/annurev-marine-120308-081019

Moore, W. S., & Arnold, R. (1996). Measurement of ^{223}Ra and ^{224}Ra in coastal waters using a delayed coincidence counter. *Journal of Geophysical Research*, *101*(C1), 1321–1329. https://doi.org/10.1029/95JC03139

Moore, W. S., Beck, M., Riedel, T., van der Loeff, M. R., Dellwig, O., Shaw, T. J., et al. (2011). Radium-based pore water fluxes of silica, alkalinity, manganese, DOC, and uranium: A decade of studies in the German Wadden Sea. *Geochimica et Cosmochimica Acta*, *75*(21), 6535–6555. https://doi.org/10.1016/j.gca.2011.08.037

Moore, W. S., & Krest, J. (2004). Distribution of ^{223}Ra and ^{224}Ra in the plumes of the Mississippi and Atchafalaya Rivers and the Gulf of Mexico. *Marine Chemistry*, *86*(3-4), 105–119. https://doi.org/10.1016/j.marchem.2003.10.001

O'Connor, A. E., Krask, J. L., Canuel, E. A., & Beck, A. J. (2018). Seasonality of major redox constituents in a shallow subterranean estuary. *Geochimica et Cosmochimica Acta*, *224*, 344–361. https://doi.org/10.1016/j.gca.2017.10.013

Porcelli, D. (2008). Chapter 4 Investigating groundwater processes using U- and Th-series nuclides. In S. Krishnaswami & J. K. Cochran (Eds.), *Radioactivity in the environment* (pp. 105-153). Oxford, UK: Elsevier.

Porcelli, D., & Swarzenski, P. W. (2003). The behavior of U- and Th-series nuclides in groundwater. *Reviews in Mineralogy and Geochemistry*, *52*, 317–361. https://doi.org/10.2113/0520317

Rama, & Moore, W. S. (1996). Using the radium quartet for evaluating groundwater input and water exchange in salt marshes. *Geochimica et Cosmochimica Acta*, *60*(23), 4645–4652. https://doi.org/10.1016/S0016-7037(96)00289-X

Robinson, C., Li, L., & Barry, D. A. (2007). Effect of tidal forcing on a subterranean estuary. *Advances in Water Resources*, *30*(4), 851–865. https://doi.org/10.1016/j.advwatres.2006.07.006

Robinson, C. E., Xin, P., Santos, I. R., Charette, M. A., Li, L., & Barry, D. A. (2018). Groundwater dynamics in subterranean estuaries of coastal unconfined aquifers: Controls on submarine groundwater discharge and chemical inputs to the ocean. *Advances in Water Resources*, *115*, 315–331. https://doi.org/10.1016/j.advwatres.2017.10.041

Rouxel, O., Sholkovitz, E., Charette, M., & Edwards, K. J. (2008). Iron isotope fractionation in subterranean estuaries. *Geochimica et Cosmochimica Acta*, *72*(14), 3413–3430. https://doi.org/10.1016/j.gca.2008.05.001

Santos, I. R., Burnett, W. C., Chanton, J., Mwashote, B., Suryaputra, I. G., & Dittmar, T. (2008). Nutrient biogeochemistry in a Gulf of Mexico subterranean estuary and groundwater-derived fluxes to the coastal ocean. *Limnology and Oceanography*, *53*(2), 705–718. https://doi.org/10.4319/lo.2008.53.2.0705

Santos, I. R., Burnett, W. C., Dittmar, T., Suryaputra, I. G. N. A., & Chanton, J. (2009). Tidal pumping drives nutrient and dissolved organic matter dynamics in a Gulf of Mexico subterranean estuary. *Geochimica et Cosmochimica Acta*, *73*(5), 1325–1339. https://doi.org/10.1016/j.gca.2008.11.029

Santos, I. R., Eyre, B. D., & Huettel, M. (2012). The driving forces of porewater and groundwater flow in permeable coastal sediments: A review. *Estuarine, Coastal and Shelf Science*, *98*, 1–15. https://doi.org/10.1016/j.ecss.2011.10.024

Swarzenski, P. W. (2007). U/Th series radionuclides as coastal groundwater tracers. *Chemical Reviews*, *107*(2), 663–674. https://doi.org/10.1021/cr0503761

Swarzenski, P. W., Reich, C., Kroeger, K. D., & Baskaran, M. (2007). Ra and Rn isotopes as natural tracers of submarine groundwater discharge in Tampa Bay, Florida. *Marine Chemistry*, *104*(1-2), 69–84. https://doi.org/10.1016/j.marchem.2006.08.001

Tao, Y., Dan, D., Xuejiao, H., Changda, H., Guo, F., & Fengchang, W. (2019). Characterization of phosphorus accumulation and release using diffusive gradients in thin films (DGT)—Linking the watershed to Taihu Lake, China. *Science of the Total Environment*, *673*, 347–356. https://doi.org/10.1016/j.scitotenv.2019.04.102

Tricca, A., Porcelli, D., & Wasserburg, G. J. (2000). Factors controlling the groundwater transport of U, Th, Ra, and Rn. *Journal of Earth System Science*, *109*, 95–108. https://doi.org/10.1007/BF02719153

Tricca, A., Wasserburg, G. J., Porcelli, D., & Baskaran, M. (2001). The transport of U- and Th-series nuclides in a sandy unconfined aquifer. *Geochimica et Cosmochimica Acta*, *65*(8), 1187–1210. https://doi.org/10.1016/S0016-7037(00)00617-7

Wang, X., Li, H., Zheng, C., Yang, J., Zhang, Y., Zhang, M., et al. (2018). Submarine groundwater discharge as an important nutrient source influencing nutrient structure in coastal water of Daya Bay, China. *Geochimica et Cosmochimica Acta*, *225*, 52–65. https://doi.org/10.1016/j.gca.2018.01.029

Webster, I. T., Hancock, G. J., & Murray, A. S. (1994). Use of radium isotopes to examine pore-water exchange in an estuary. *Limnology and Oceanography*, *39*(8), 1917–1927. https://doi.org/10.4319/lo.1994.39.8.1917

Webster, I. T., Hancock, G. J., & Murray, A. S. (1995). Modeling the effect of salinity on radium desorption from sediments. *Geochimica et Cosmochimica Acta*, *59*(12), 2469–2476. https://doi.org/10.1016/0016-7037(95)00141-7

Zhang, Y., Li, H. L., Xiao, K., Wang, X. J., Lu, X. T., Zhang, M., et al. (2017). Improving estimation of submarine groundwater discharge using radium and radon tracers: Application in Jiaozhou Bay, China. *Journal of Geophysical Research: Oceans*, *122*, 8263–8277. https://doi.org/10.1002/2017JC013237

Erratum

In the originally published version of this article, Equation (1) contained a formatting error. The equation has since been corrected and this version may be considered the authoritative version of record.